

## **Title: OpenMAP-T1: A Rapid Deep Learning Approach to Parcellate 280 Anatomical Regions to Cover the Whole Brain**

Kei Nishimaki<sup>1,2</sup>, Kengo Onda<sup>1</sup>, Kumpei Ikuta<sup>2</sup>, Yuto Uchida<sup>1</sup>, Susumu Mori<sup>1</sup>, Hitoshi Iyatomi<sup>3</sup>, and Kenichi Oishi<sup>1,3#</sup>

for the Alzheimer's Disease Neuroimaging Initiative\* and the Australian Imaging Biomarkers and Lifestyle flagship study of aging\*\*

#Corresponding Author. Kenichi Oishi ([koishi2@jhmi.edu](mailto:koishi2@jhmi.edu))  
720 Rutland Ave. 208 Traylor Building, Baltimore, MD, 21205, USA

<sup>1</sup>The Russell H. Morgan Department of Radiology and Radiological Science, The Johns Hopkins University School of Medicine, Baltimore, MD, USA

<sup>2</sup> Department of Applied Informatics, Graduate School of Science and Engineering, Hosei University, Tokyo, Japan

<sup>3</sup> The Richman Family Precision Medicine Center of Excellence in Alzheimer's Disease, Johns Hopkins University School of Medicine, Baltimore, MD, USA

\*Data used in preparation of this article were obtained from the Alzheimer's Disease Neuroimaging Initiative (ADNI) database ([adni.loni.usc.edu](http://adni.loni.usc.edu)). As such, the investigators within the ADNI contributed to the design and implementation of ADNI and/or provided data but did not participate in the analysis or writing of this report. A complete listing of ADNI investigators can be found at: [http://adni.loni.usc.edu/wp-content/uploads/how\\_to\\_apply/ADNI\\_Acknowledgement\\_List.pdf](http://adni.loni.usc.edu/wp-content/uploads/how_to_apply/ADNI_Acknowledgement_List.pdf)

\*\*Data used in the preparation of this article was obtained from the Australian Imaging Biomarkers and Lifestyle flagship study of ageing (AIBL) funded by the Commonwealth Scientific and Industrial Research Organisation (CSIRO), which was made available at the ADNI database ([www.loni.usc.edu/ADNI](http://www.loni.usc.edu/ADNI)). The AIBL researchers contributed data but did not participate in the analysis or writing of this report. AIBL researchers are listed at [www.aibl.csiro.au](http://www.aibl.csiro.au).

**Keyword:** Brain, MRI, T1, parcellation, segmentation, deep-learning

## 0. Abstract

This study introduces OpenMAP-T1, a deep-learning-based method for rapid and accurate whole-brain parcellation in T1-weighted brain MRI, which aims to overcome the limitations of conventional normalization-to-atlas-based approaches and multi-atlas label-fusion (MALF) techniques. Brain image parcellation is a fundamental process in neuroscientific and clinical research, enabling a detailed analysis of specific cerebral regions. Normalization-to-atlas-based methods have been employed for this task, but they face limitations due to variations in brain morphology, especially in pathological conditions. The MALF techniques improved the accuracy of the image parcellation and robustness to variations in brain morphology, but at the cost of high computational demand that requires a lengthy processing time. OpenMAP-T1 integrates several convolutional neural network models across six phases: preprocessing; cropping; skull-stripping; parcellation; hemisphere segmentation; and final merging. This process involves standardizing MRI images, isolating the brain tissue, and parcellating it into 280 anatomical structures that cover the whole brain, including detailed gray and white matter structures, while simplifying the parcellation processes and incorporating robust training to handle various scan types and conditions. The OpenMAP-T1 was tested on eight available open resources, including real-world clinical images, demonstrating robustness across different datasets with variations in scanner types, magnetic field strengths, and image processing techniques, such as defacing. Compared to existing methods, OpenMAP-T1 significantly reduced the processing time per image from several hours to less than 90 seconds without compromising accuracy. It was particularly effective in handling images with intensity inhomogeneity and varying head positions, conditions commonly seen in clinical settings. The adaptability of OpenMAP-T1 to a wide range of MRI datasets and its robustness to various scan conditions highlight its potential as a versatile tool in neuroimaging.

# 1. Introduction

Brain image parcellation constitutes a pivotal aspect of neuroscientific and clinical investigations, delineating a repertoire of parcels that correspond to biologically or functionally pertinent cerebral units. These defined parcels facilitate quantitative analyses of neuroimaging data for each individual region [1-19]. While numerous criteria exist for the parcellation of cerebral territories, the designation of regional labels predominantly relies on established anatomical or neurofunctional insights. Examples include macroanatomical landmarks, such as gyri and sulci [10-12, 16, 19, 20], cellular configurations at the microscopic scale [20], the spatial distribution of transporters or receptors [21, 22], and regions characterized by vascular territories [23], as well as by functional or anatomical connectivity [5, 24-29].

The electronic version of brain atlases frequently serves as a reference for demarcating anatomical or functional territories. Such atlases typically comprise a standard brain image paired with an accompanying parcellation map, annotated with labels spanning the entirety of the cortex, white matter areas, or entire brain regions. Within atlas-based analyses, the inherent semantic information encapsulated within the parcellation map is transposed onto the target brain image for subsequent image quantification. Diverse atlas types have been formulated and employed for brain image parcellation (see [10, 16, 18, 19] for details). Image transformation techniques enable the adjustment of these knowledge-informed parcels from the atlas to conform to the specificities of the target brain. Herein, the atlas undergoes mathematical transformation ("warping" or "deformation") to be congruent with the morphological attributes of the target brain, thus generating a parcellation map in harmony with the target's morphology. This technique boasts over two decades of application. However, due to the pronounced individual variations in brain morphology, substantial discrepancies can sometimes be observed between the target and atlas brain structures. These mismatches make precise atlas-to-target transformations challenging [9, 30]. Notably, these transformation errors are exacerbated when addressing neuroimages of brains with pathological atrophy, lesions exhibiting signal alterations, such as ischemic or hemorrhagic lesions, or mass lesions [31]. Consequently, it has become clear that relying solely on a single brain atlas for accurate parcellation is not viable. To adeptly segment an array of brains, and encompass those that are pathologically affected, the multi-atlas label-fusion (MALF) techniques [32-39] have garnered significant traction since the 2010s.

In the MALF approach, typically 10-30 atlases are curated and subsequently transformed to the target brain. These atlases are carefully chosen to encompass a diverse range of morphological features, ensuring accommodation for inter-individual variations in cerebral morphology. This leads to the generation of as many parcellation maps as the number of atlases employed as intermediate products, each reflecting subtle differences attributable to the unique characteristics of its corresponding atlas. Leveraging these multiple parcellation outputs, a series of mathematical techniques, termed 'label fusion,' are employed to integrate and obtain a final optimal parcellation map for the target brain [33]. This resultant map showcases superior accuracy compared to one obtained from a single atlas [34]. Consequently, the MALF approach has found significant utility, especially in the precise parcellation of brains affected by neurodegenerative disorders that cause atrophy [39].

Given the proficiency of the MALF approach in accurately segmenting a diverse range of pathologically affected brains, its application in quantifying clinical imaging datasets that comprise various diseases seems an intuitive progression. For instance, parcellating clinical brain MRI data can yield volumetric insights into distinct cerebral regions, facilitating diagnosis,

analogous image retrieval, and autonomous detection of characteristics that deviate from normative brain parameters. Nonetheless, the MALF techniques are characteristically computationally intensive, necessitating intricate mathematical transformations across multiple atlases, followed by label fusion. Consider MRICloud [38], a freely accessible cloud-based computational tool renowned for its precise brain MRI parcellation with multi-atlas label fusion. Despite the use of a cluster computing infrastructure environment, optimized for parallel processing, the use of the computationally intensive advanced large deformation diffeomorphic metric mapping for image transformation results in several hours of processing time for a single image. This computational burden poses significant challenges in big-data analysis or clinical scenarios. For instance, in clinical settings where multiple brain MRI scans necessitate immediate segmentation for diagnostic assistance or when a large repository of brain images requires quantification, expedited processing is imperative. Under such circumstances, the current MALF techniques prove overly resource-intensive and time-prohibitive.

In recent years, there has been a growing inclination to use deep-learning models to expedite the parcellation of brain MRI while simultaneously enhancing accuracy [40-47]. For instance, ParcelCortex [45] employs convolutional neural networks (CNNs), while DeepParcellation [46] integrates the Attention 3D U-Net for cortical segmentation based on the Desikan-Killiany-Tourville atlas parcellation derived from FreeSurfer [48]. A salient advantage of deep-learning lies in its efficiency: once a model is trained and validated, it permits rapid parcellation. This proficiency renders it advantageous for processing extensive datasets, encompassing both research-oriented and clinical imaging. Nonetheless, models capable of detailed segmentation across all cerebral regions, inclusive of white matter territories, and those offering results comparable to the sophisticated MALF method, remain underdeveloped.

In the present study, we introduce a deep-learning-based, rapid, whole-brain parcellation method. Our aim was to construct a model that not only mirrors the accuracy of the multi-atlas approach, but also accommodates images from diverse repositories and facilitates parcellation within mere minutes on a standard desktop configuration. The model has been named "Open resource for Multiple Anatomical structure Parcellation for T1-weighted brain MRI (OpenMAP-T1)" and is accessible through the website (URL: <https://github.com/OishiLab/OpenMAP-T1>).

Table 1. Dataset used in our study: Alzheimer's Disease Neuroimaging Initiative 2/3 (ADNI2/ADNI3), Australian Imaging, Biomarkers and Lifestyle (AIBL), Calgary-Campinas-12 (CC-12), LONI Probabilistic Brain Atlas (LPBA40), Neurofeedback Skull-stripped (NFBS) Repository, Open Access Series of Imaging Studies 1/4 (OASIS1/OASIS4). OASIS4 consists of clinical MRIs with various diseases and conditions. OpenMAP-T1 was trained using only 350 cases in ADNI2. AD, Alzheimer's disease; MCI, mild cognitive impairment; CN, cognitively normal older people. One MRI per subject was randomly selected to avoid potential bias.

Dataset		Train		Test						
		ADNI2	ADNI2	ADNI3	AIBL	CC359	LPBA40	NFBS	OASIS1	OASIS4
# Subjects		350	750	929	376	359	40	125	235	570
# Voxels ( $mm^3$ )		1.05~1.43	1.05~2.18	0.99~1.44	1.19~1.20	0.79~1.33	0.91~1.10	0.99	1.25	0.22~1.52
Age	mean	73.7	74.3	73.7	74.0	53.4	29.2	31.0	72.3	72.5
	std	7.4	7.5	8.0	7.1	7.8	6.3	6.6	12.0	9.2
Sex	F	160	353	486	198	183	20	77	156	303
	M	190	397	443	178	176	20	48	79	267
Manufacturer	GE	97	254	211		120	40			
	PHILIPS	65	126	142		119				
	SIEMENS	188	370	576	376	120		125	235	570
Field Strength	1.5T	30	149		102	179	40		235	29
	3T	320	601	929	274	180		125		541
Diagnosis	CN	122	259	522	268	359	40	125	135	
	MCI	196	318	301	64					
	AD	32	173	106	44				100	

Real-World MRI

## 2. Materials and Methods

### 2.1. Participants

We used public brain MRI datasets for the model training and evaluations: Alzheimer's Disease Neuroimaging Initiative 2 and 3 (ADNI2/ADNI3) [49], Australian Imaging, Biomarkers and Lifestyle (AIBL) [50, 51], Calgary-Campinas-359 (CC-359) [52], LONI Probabilistic Brain Atlas (LPBA40) [53], Neurofeedback Skull-stripped (NFBS) [54], and Open Access Series of Imaging Studies 1 and 4 (OASIS1/OASIS4) [55, 56]. Table 1 shows the dataset descriptions used in this study. Three-hundred-fifty baseline MRIs of ADNI2 were used to train the OpenMAP-T1, and other MRIs, including 750 ADNI2. MRIs not used to train the model were used to test the model. Although these datasets include multiple scans from single participants, only one MRI per participant was randomly selected to avoid potential bias toward specific individuals.

The ADNI [49] was launched in 2003 as a public-private partnership, led by Principal Investigator Michael W. Weiner, MD. The primary goal of ADNI has been to test whether serial magnetic resonance imaging (MRI), positron emission tomography (PET), other biological markers, and clinical and neuropsychological assessment can be combined to measure the progression of mild cognitive impairment (MCI) and early Alzheimer's disease (AD). For up-to-date information, see [www.adni-info.org](http://www.adni-info.org). The ADNI study has evolved through several phases, with ADNI2 during 2011 - 2016 and ADNI3 during 2016 - 2022 being two of them. For our study, we have included Magnetization Prepared Rapid Acquisition Gradient Echo (MPRAGE) images from ADNI2 and ADNI3 datasets. As recommended by the ADNI team, we included ADNI2 MPRAGE images (ADNI2: 55.1-94.7 years, ADNI3: 50.5-97.4 years) preprocessed with Gradwarp, B1 non-uniformity, and N3 bias field corrections. Note that the preprocessing was not required for the ADNI3 MPRAGE images since, such corrections are internally applied by individual vendors.

The AIBL [50, 51], also known as Australian ADNI, is a long-term research initiative that aims to understand the biomarkers and cognitive characteristics that determine the development of AD. The AIBL study commenced in 2006 and the methodology has been reported previously [50]. In our study, the the original MPRAGE images (55.0-96.0 years) downloaded from the website (<https://aibl.org.au/>) were included.

The CC359 [52] dataset is an open, multi-vendor, multi-field-strength brain MRI dataset. It is composed of 359 MRIs of healthy adults acquired on scanners from three vendors (Siemens, Philips, and General Electric (GE)) at both 1.5 T and 3 T to evaluate the impact of scanner vendor and magnetic field strength on skull-stripping. In our study, we used MPRAGE images of Siemens and Philips and 3D spoiled gradient echo sequence (SPGR) (29.0-80.0 years) on the GE, downloaded from the website (<https://www.ccdataset.com/download>).

The LPBA40 [53] is a set of brain MRIs of 40 healthy young adults scanned on a single 1.5T GE scanner. In our study, we used the 3D SPGR images (19.3-39.5 years) downloaded from the website ([https://www.loni.usc.edu/research/atlas\\_downloads](https://www.loni.usc.edu/research/atlas_downloads)).

The NFBS [54] dataset is a repository of brain MRIs of 125 individuals, including 66 who were diagnosed with a wide range of psychiatric disorders, scanned on a single 3T Siemens scanner. In

our study, we used MPRAGE images (21.0-45.0) downloaded from the website ([http://preprocessed-connectomes-project.org/NFB\\_skullstripped/](http://preprocessed-connectomes-project.org/NFB_skullstripped/)).

The OASIS [55, 56] is a brain MRI dataset that includes multiple releases, such as OASIS-1, OASIS-2, OASIS-3, and OASIS-4, which provide cross-sectional and longitudinal MRI data for normal aging and AD. The subjects of the OASIS1 were selected from a larger database of individuals who had participated in MRI studies at Washington University. OASIS4 is a Clinical Cohort and was acquired at the Memory Diagnostic Center. All subjects in OASIS4 underwent a clinical assessment conducted by experienced clinicians. The 570 subjects we selected included 16 different diagnostic labels. In our study, we used MPRAGE images (OASIS1: 33.0-96.0, OASIS4: 37.0-94.0) downloaded from the website (<https://www.oasis-brains.org/>).

## 2.2. Anatomical Labeling for Training and Evaluation

The parcellation map obtained from the MALF algorithm [57, 58] and implemented in MRICloud ([www.MRICloud.org](http://www.MRICloud.org) Johns Hopkins University, Baltimore, MD, USA) [38] was used to generate anatomical labels for model training and evaluation. The MALF algorithm parcellates the entire brain into 280 brain regions. We went over the 350 MRIs used as a training dataset to confirm that there was no substantial mislabeling; therefore, manual correction was not performed. Details of the labels used to train OpenMAP-T1 are shown in Figure A in the Supplementary Material. It should be noted that, in this paper, the term 'MALF' will henceforth refer exclusively to the specific algorithm implemented in MRICloud.

## 2.3. Model Design

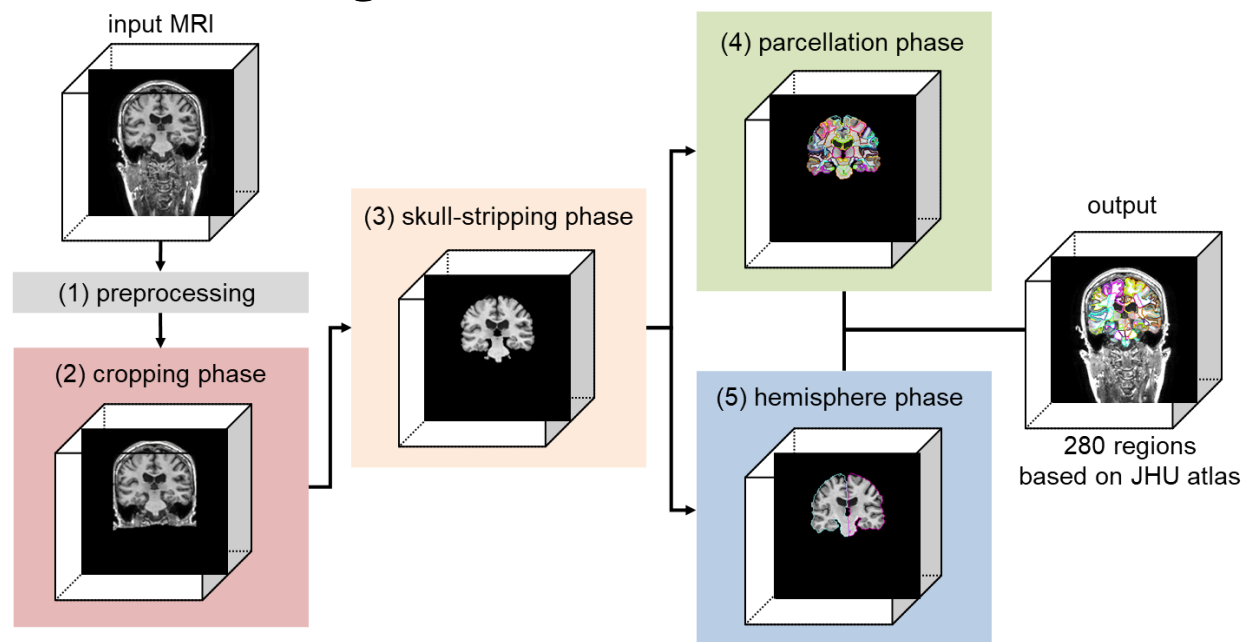


Figure 1. Overview of the open resource for multiple anatomical structure parcellation for T1-weighted brain MRI (OpenMAP-T1) consisting of the preprocessing, cropping phase, skull-stripping phase, parcellation phase, and hemisphere phase.

The OpenMAP-T1 was designed to accept any T1-weighted images and output a corresponding parcellation map, in which gray matter, white matter, and cerebrospinal fluid areas are segmented and further parcellated into 280 anatomical regions based on the JHU-atlas [10].

Figure 1 shows the overview of OpenMAP-T1. The OpenMAP-T1 follows six phases: (1) preprocessing; (2) application of a cropping network (CNet) consisting of the 2D U-Net [59] to crop the area surrounding the head in the input MRI; (3) application of a skull-stripping network (SSNet) consisting of the 2D U-Net to extract the brain; (4) application of a parcellation network (PNet) consisting of the 2.5D U-Net [60] to parcellate the whole brain into 141 anatomical areas; (5) application of a hemisphere network (HNet) consisting of 2D U-Net to segment the whole brain into the right and left hemisphere; and (6) separation of 139 regions of the 141 from the parcellation map created in phase (4) into right and left sides based on the hemisphere map from phase (5), with the exception of the 3rd and 4th ventricles. Consequently, OpenMAP -T1 produces a parcellation map consisting of 280 neuroanatomically defined regions.

### 2.4.1. Preprocessing

N4 bias field correction [61] was applied to remove intensity non-uniformity. In addition, the images were rescaled to a resolution of  $1 \times 1 \times 1$  mm using trilinear interpolation, and their size was standardized to  $256 \times 256 \times 256$  through the application of zero padding. Pixels with intensity values below 0 or above  $u+2\sigma$  (where  $u$  is the mean and  $\sigma$  is the standard deviation) were identified as outliers and excluded. These pixels were then linearly normalized to a range between -1 and 1. Following normalization, the excluded pixels were replaced with the minimum and maximum values within this normalized range.

### 2.4.2 Cropping phase

Non-brain soft tissue, such as skin, fat, and muscle, potentially confound whole-brain parcellation. In particular, variations in the intensity of the neck tissue interferes with image segmentation. In addition, the extent to which the field-of-view of the image covers the neck depends on the scan parameters, and, in some publicly available datasets (e.g., NFBS and OASIS1), a defacing algorithm was applied to the image for de-identification [54, 55]. To reduce the influence of neck tissue in image segmentation and parcellation, we set the cropping phase to eliminate the regions below the brain in a consistent way using the CNet. Figure B in the Supplementary Materials shows an overview of the cropping phase and the detail of the CNet is shown in Section 2.4.6.

In the training of the CNet, the head region included in the parcellation map resulting from MALF was used (Figure A in the Supplementary Material), since the parcellation map covers the head above the foramen magnum, and does not include neck tissue below it. The CNet employed 2D segmentation on individual cross-sections of a 3D brain MRI, which were then vertically stacked for high-speed processing. By utilizing the 2D U-Net architecture, it was possible to train the model using numerous images from a single MRI. For example, with a  $256 \times 256 \times 256$  matrix, 2D U-Net can utilize 256 slices from a single MRI. Note that the cropping phase was specifically designed to eliminate tissue located below the brain; hence, the axial section, which does not contain vertical information, was excluded from the ensemble. The output is a probability map for the head above the foramen magnum, and areas with a probability of 50% or higher are defined as head masks. A failure in the cropping phase considerably affects the

processing performance of subsequent phases. To prevent small gaps or missing areas in the output mask, a closing process was applied using a  $3 \times 3 \times 3$  filter. The dilation and erosion operations were performed three times each.

### **2.4.3. Skull-stripping phase**

To further remove signals from extracranial soft tissues that remain after the initial cropping phase, we applied skull-stripping to the image. Given the varying intensity ranges caused by different scanner types, scan sequences, and parameters, it is essential to adjust the image contrast between gray and white matter, as well as cerebrospinal fluid. However, signals from extracranial soft tissues, such as fat, bone, and muscle, vary greatly and can disrupt the stable signal intensity profile of intracranial structures. This variation can adversely affect the performance of deep-learning models. By employing skull-stripping with SSNet, we effectively removed irrelevant regions for the later stages of parcellation and hemisphere analysis. Figure C in the Supplementary Materials provides an overview of the skull-stripping phase and the detail of the SSNet is shown in Section 2.4.6.

To develop SSNet, we trained the model using an intracranial mask obtained from MALF (Figure A in the Supplementary Material). SSNet performs 2D segmentation on any cross-sectional view of a 3D brain MRI, stacking these sections vertically in a manner similar to that of CNet. We input three cross-sectional views—sagittal, coronal, and axial—into a 2D-U-Net. The output is a label for the intracranial space, defined as areas with a probability of 50% or higher.

### **2.4.4. Parcellation phase**

In our current computing environment, training a full-size deep-learning network for multi-class parcellation with 3D images, such as an entire brain, presented challenges. To optimize parcellation performance without running GPU memory, we used two strategies: utilizing 2D slices, and merging the left and right brain regions. An overview of the parcellation phase can be seen in Figure D of the Supplementary Materials.

The PNet, designed for 2D segmentation of 3D brain MRI cross-sections, stacks these sections vertically. It is important to note that the PNet functions as a 2.5D U-Net, incorporating a target slice and the slices directly above and below it, and combining these slices along the channel direction. In typical 2D U-Net applications for 3D images, vertical spatial information is lost. However, the 2.5D U-Net approach allows for the use of pseudo spatial information while reducing parameter count compared to a 3D U-Net. Consequently, for each cross-section, three image slices ( $256 \times 256$ ) are stacked in the depth direction, resulting in an input dimension of  $256 \times 256 \times 3$  for the PNet. The choice to stack three slices was based on the findings from preliminary experiments. Furthermore, of the 280 brain regions, those present in both hemispheres were merged as a single region (Figure A in the Supplementary Material). Excluding the 3rd and 4th ventricles, 278 regions exist in both the left and right hemispheres, as per the JHU-atlas. During the parcellation phase, this merging reduces the target regions for PNet to 141, making the segmentation task effectively 142 classes, including the background.

Combining the left and right regions offers three benefits. First, it enables U-Net to train on larger regions, which is crucial as some of the 280 regions are smaller than 100 voxels and challenging to extract accurately. Merging hemispheres roughly doubles the volume of these

regions, making them more tractable. Second, it reduces computational costs. In 2D or 2.5D U-Net, the dimension of the output parcellation map is height  $\times$  width  $\times$  channels (number of segmentation classes). By merging hemispheres, we halve the number of output channels. Third, it facilitates the use of sagittal sections. Normally, distinguishing left from right in sagittal sections is tough, and can potentially degrade parcellation performance. This issue is resolved by treating the hemispheres as identical.

Unlike CNet and SSNet, PNet uses three models for each cross-section (coronal, sagittal, axial), and the final prediction is based on the highest average prediction probability across these models. This approach was chosen to ensure consistent predictions in regions where parcellation is challenging, such as at the brain's edges. Training a single model with three cross-sections risks misidentifications, like mistaking a coronal for an axial section.

### **2.4.5. Hemisphere phase**

The segmentation task of HNet is a three-class classification: background; right hemisphere; and left hemisphere. This classification aims to determine the left and right borders of 139 of the 141 region labels generated in the parcellation phase. The hemisphere phase model was trained using hemisphere labels obtained from MALF. An overview of this phase is depicted in Figure E of the Supplementary Materials and the detail of the HNet is shown in Section 2.4.6.

HNet employs 2D segmentation on any cross-section, stacking these sections vertically. It specifically uses axial and coronal sections to output the hemisphere labels. A post-processing step involving dilation was implemented to separate each region generated during the parcellation phase to the right and left sides. The process is as follows: (1) Dilate only the left hemisphere label. (2) Modify the overlapping parts of the dilated left hemisphere label with the right hemisphere label to be classified as right side. (3) Dilate only the right hemisphere label. (4) Modify the overlapping parts of the dilated right hemisphere label with the left hemisphere label to be classified as left side. This method allows the hemisphere labels to expand while minimally impacting the borders.

Finally, the parcellation map, which includes 280 region labels, was created by dividing the 141-region parcellation map into left and right hemispheres, using the hemisphere labels obtained from the hemisphere phase. It is important to note that in the 141-region parcellation map, the two regions without a left-right distinction (3rd and 4th ventricles) were given priority over the hemisphere labels (i.e., the hemisphere label was ignored). Furthermore, if there was an overlap between the background from the parcellation phase and the hemisphere region from the hemisphere phase, the background was given precedence.

### **2.4.6. Structures of CNet, SSet, PNet, and HNet and their training**

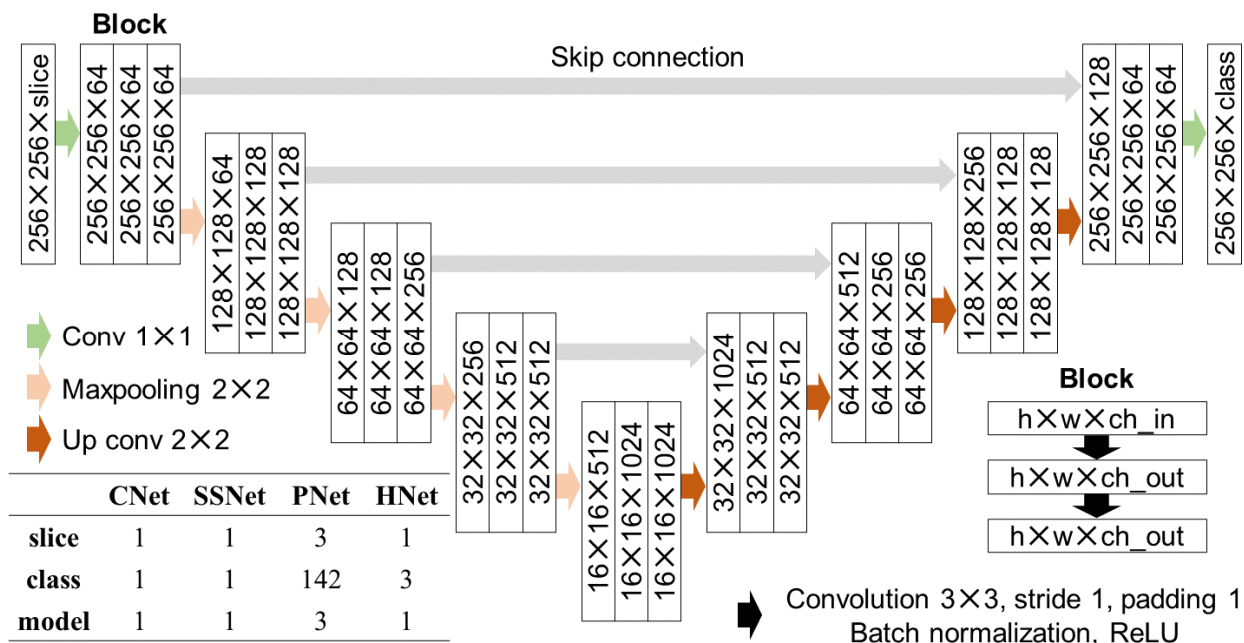


Figure 2. Architecture of the U-Net (CNet, SSNet, PNet, and HNet). U-Net consists of nine blocks, and each block includes two convolutions, batch normalization, and a ReLU function. The CNet, SSNet, and HNet have one input channel, and only PNet has three channels, including the target slice and its upper and lower slices. Since the CNet and SSNet perform binary cross entropy, the output class is only one. Also, since the PNet and HNet use multi-class classification, the output is the number of regions plus one (background). Note that only PNet has three models (for coronal, sagittal, and axial sections).

The CNet, SSNet, PNet, and HNet each comprise 24 convolution layers based on 2D CNN (Figure 2). The main distinction between them lies in the number of input and output channels. As detailed in Figure 2, CNet, SSNet, and HNet had one input channel, while PNet had three channels.

Data augmentation included a random rotation ranging from -20 to +20 degrees and a random shift from -20 to +20 pixels, applied with an 80% probability. For the sagittal cross-sections, a broader random rotation range of -30 to +30 degrees was used, based on the greater variation seen on existing MRI databases. To ensure robust performance for low signal-to-noise ratio (SNR) images, random Gaussian noise (mean 0, standard deviation 0.25) was added with a 50% probability. These data augmentation techniques were applied consistently across all phases. MRI magnetic field inhomogeneity led to very low-frequency intensity variations throughout the image. Consequently, a random bias field [62] was introduced with a 50% probability during the cropping and skull-stripping phases. While N4 bias field correction was used in preprocessing to address inhomogeneity as much as possible, this data augmentation was implemented to enhance the model's robustness. To adapt the CNet for use with images that did not include the neck area below the foramen magna, commonly found in axial scans and defaced images, we augmented the training data by incorporating images with the neck area cropped out, at a probability of 20%. Similar to CNet, the training dataset for SSNet was augmented by including skull-stripped images as inputs with a 20% probability. This approach enables the model to more accurately identify the location of the brain by reducing the impact of non-brain regions.

The CNet, SSNet, PNet, and HNet were mainly trained using two RTX 3090 graphics processing units (GPU) with 24GB memory for about 24 hours. Also, Automatic Mixed Precision (AMP) was utilized to accelerate training. The number of epochs was set to 10,000, and the learning rate was set to decrease sequentially from 0.01 to 0.0001 by the Cosine Annealing Learning Rate Scheduler. The batch size was 64 on CNet, SSNet, and HNet, and 32 on PNet. For the loss functions, the CNet and SSNet used binary cross-entropy, while the PNet used a combination of cross-entropy and Dice loss. The HNet exclusively used cross-entropy.

## **2.5. Evaluation of parcellation performance**

We assessed the effectiveness of OpenMAP-T1 in terms of technical and biological criteria. The technical assessment encompassed three areas: parcellation performance; generalizability; and processing time. For the biological evaluation, OpenMAP-T1 was tested under the assumption of its application in AD research. Furthermore, we compared the parcellation accuracy of OpenMAP-T1 with that of FreeSurfer (version 7.4.1), a widely used tool in brain MRI parcellation.

### **2.5.1. Technical evaluation**

#### **Parcellation performance**

To evaluate the parcellation performance of OpenMAP-T1, four metrics were utilized: (1) illustrate the spatial overlap between two parcellation maps generated by MALF and OpenMAP-T1 by calculating the average recall and precision, considering the results of MALF as the ground truth, and also compute the Dice score; (2) establish correlation analyses of the predicted volumes between MALF and OpenMAP-T1, indicating the consistency of the relationship between these predicted volumes, with both Pearson and Spearman correlation coefficients calculated; (3) use a Bland-Altman plot [63] to investigate agreement between regional volumes predicted by MALF and OpenMAP-T1, allowing identification of systematic bias between the measurements and outliers; and (4) analyze the relationship between the volume predicted by MALF and the corresponding Dice score, showing how the predicted volume correlates with parcellation performance. These metrics were determined for each individual region.

#### **Generalizability**

For parcellation methods to be effectively applicable in large-scale clinical research, they must possess a high degree of generalizability. To assess the generalizability of OpenMAP-T1, we examined whether significant variations in the Dice score were present based on factors such as database, scanner manufacturer, magnetic field strength, age, sex, and diagnosis. We employed analysis of variance (ANOVA) for this comparative analysis. A p-value less than 0.05 in two-sided tests was deemed to reflect statistical significance.

### **2.5.2. Comparison with FreeSurfer**

It is important to acknowledge that a direct comparison between the parcellation maps of OpenMAP-T1, which uses the JHU-atlas [10], and FreeSurfer, based on the Desikan-Killiany-Tourville (DKT) atlas [18], is not feasible because their anatomical definitions are different. Consequently, we conducted a focused comparison of OpenMAP-T1 and FreeSurfer, specifically examining the hippocampus, amygdala, and entorhinal cortex, as these regions are notably

associated with Alzheimer's Disease (AD). Two metrics were used for this comparison: (1) the average recall, precision, and Dice score for the parcellation maps of the hippocampus, amygdala, and entorhinal cortex produced by OpenMAP-T1 and FreeSurfer, considering the result of FreeSurfer as the ground truth; (2) a correlation analysis of the predicted volumes for the hippocampus, amygdala, and entorhinal cortex, comparing the results from OpenMAP-T1 and FreeSurfer.

### **2.5.3. Biological evaluation**

We assessed the diagnostic ability to distinguish between AD and CN participants using predicted volumes derived from MALF, OpenMAP-T1, and FreeSurfer. This evaluation involved 628 subjects with AD or CN labels from the ADNI3 dataset, using a three-fold cross-validation approach. A logistic regression model with Least Absolute Shrinkage and Selection Operator (LASSO) was utilized for the classification. To mitigate multicollinearity, the predicted volumes of 280 anatomical structures by MALF and OpenMAP-T1 were averaged across their left and right counterparts. Similarly, the volumes calculated by FreeSurfer for bilateral regions were also averaged. In addition, we adjusted for brain size effects by normalizing each structure's volume to the total brain volume of each participant. These normalized volumes were then transformed into z-scores, based on the mean and standard deviation, and used as input variables for the model. The classification performance was compared using the Area Under the Curve (AUC) from receiver operating characteristic (ROC) curve analysis, with significant differences determined using DeLong's algorithm [64]. A p-value less than 0.05 in two-sided tests was considered statistically significant. Furthermore, we identified the top 20 structures based on the coefficients of the LASSO model after training to understand the important regions of this model.

## **3. Results**

### **3.1. Technical evaluation**

#### **Parcellation Performance**

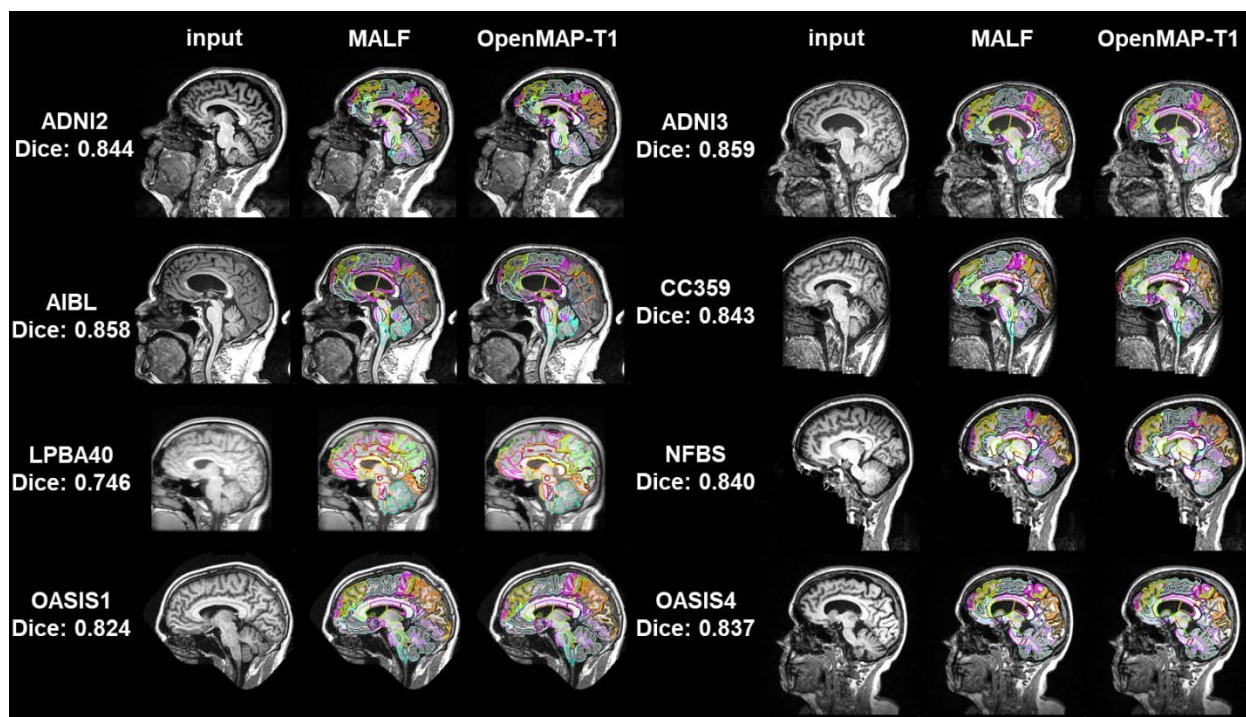


Figure 3. Representative results from MALF and OpenMAP-T1 are demonstrated. The median Dice score calculated between the two sets of results is provided. Note that defacing techniques have been implemented on NFBS and OASIS1 datasets to safeguard the privacy of the participants.

Figure 3 presents a comparative analysis of parcellation results between MALF and OpenMAP-T1. Despite significant variations in head appearance across different datasets, OpenMAP-T1 demonstrated satisfactory performance for all eight datasets. Notably, the median Dice score exceeded 0.8 for every dataset, with the exception of LPBA40, which did not utilize MPRAGE imaging.

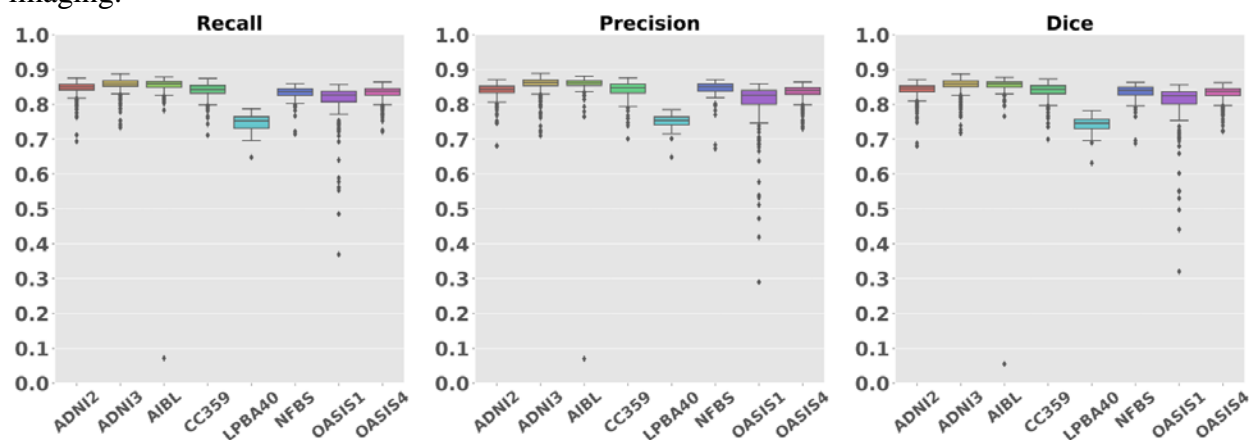


Figure 4. Boxplot of the recall, precision, and Dice scores across each dataset.

Figure 4 illustrates the average recall, precision, and Dice scores obtained from comparing 280 anatomical regions in the parcellation maps between MALF and OpenMAP-T1, considering the results of MALF as the ground truth. These scores, exceeding 0.75 in all datasets, signify a

considerable level of agreement between the two methods. However, it should be noted that some datasets displayed extreme outliers.

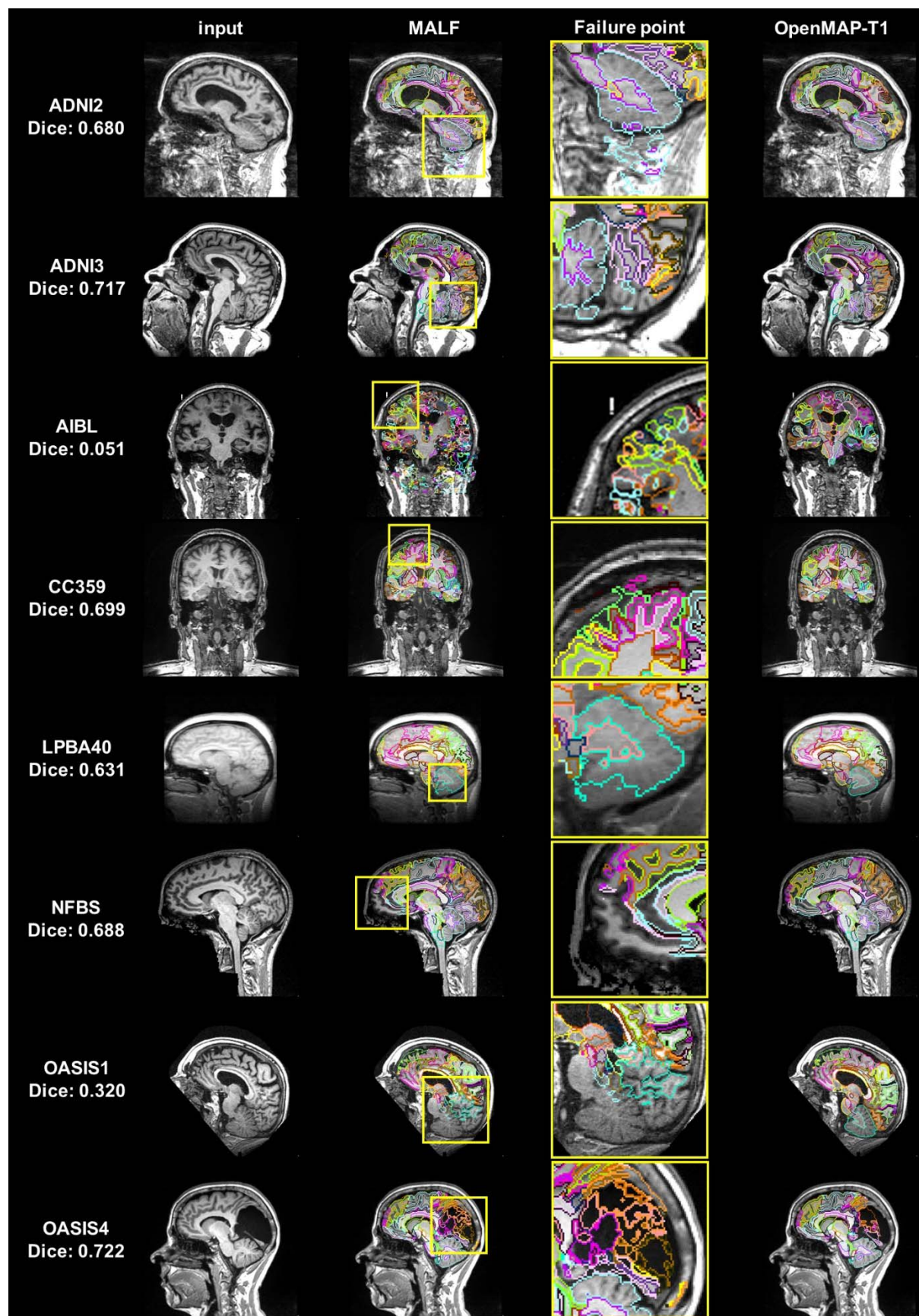


Figure 5. Image with the lowest Dice scores from all datasets (From left to right: input image, output of MALF, enlarged image of MALF failure point, output of OpenMAP-T1). The yellow squares on the images in the second column correspond to the enlarged images in the third row and highlight areas where the MALF's parcellation failed.

Figure 5 shows the image with the lowest Dice score and its underlying causes. The causes were predominantly attributed to mislabeling by MALF, except for one image from OASIS4. In the image from ADNI2, ROIs for gray and white matter in the cerebellum erroneously included neck areas. In the image from ADNI3, a portion of the occipital lobe was absent from the parcellation map. The image from AIBL was affected by extremely high-intensity noise, leading to significant mislabeling in the MALF results. In the image from CC359, the labels extended beyond the parietal lobe boundaries. In images from LPBA40 and OASIS1, parts of the cerebellum were missing in the parcellation map, a pattern also observed in other OASIS1 images. The image from NFBS had an issue with a missing section of the frontal lobe in its parcellation map. The exception was an image from OASIS4 with a large arachnoidal cyst that neither method successfully labeled.

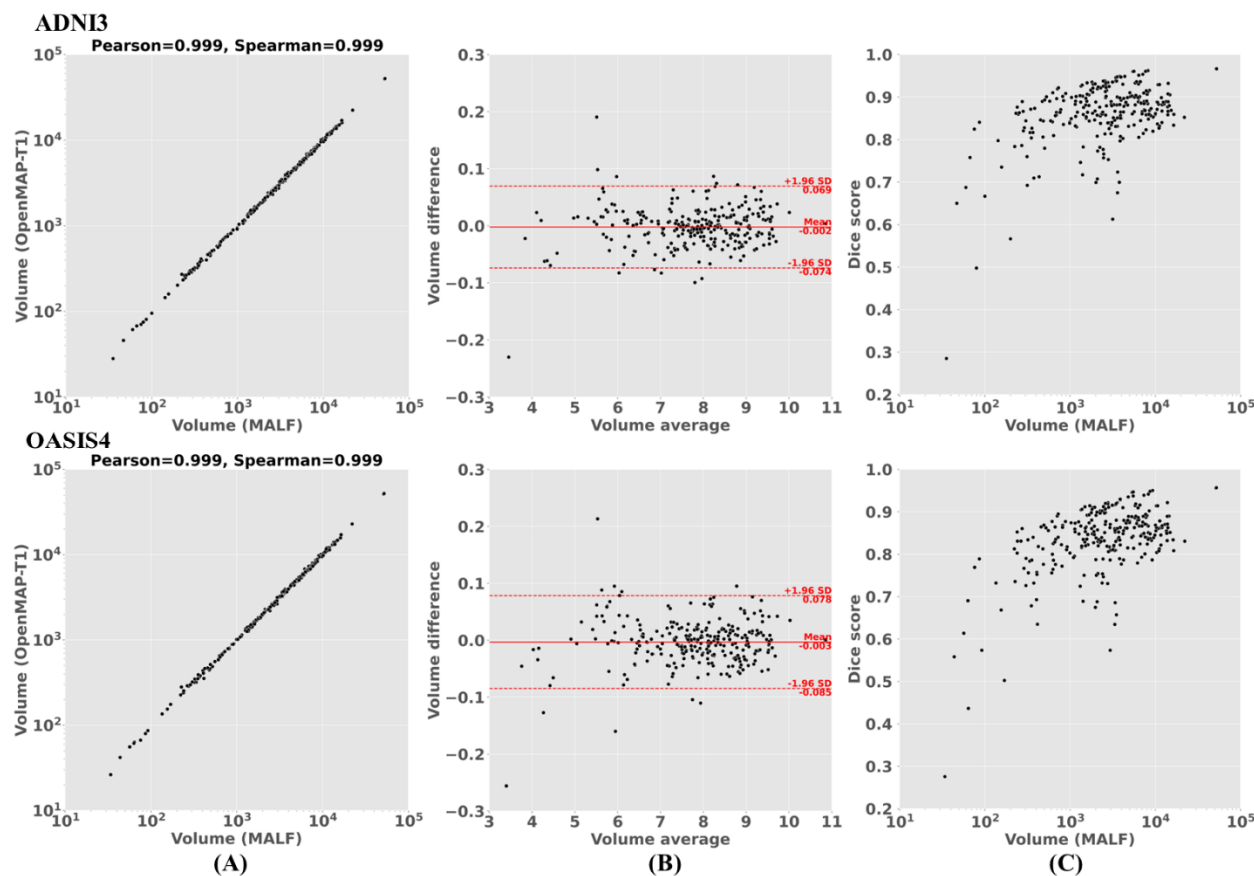


Figure 6. (A) Correlation between the predicted volumes obtained using MALF and OpenMAP-T1. (B) Bland-Altman plot to demonstrate agreement between regional volumes predicted by MALF and OpenMAP-T1. The volume measurements were transformed using a base-2 logarithmic scale. (C) Relationship between the structural volume obtained from MALF and the Dice score between MALF and OpenMAP-T1.

Figure 6A presents a comparison of the region volumes predicted by MALF and OpenMAP-T1 for the ADNI3 and OASIS4 databases. The correlation coefficients for these comparisons were above 0.99 using both Pearson and Spearman methods, indicating an almost perfect correlation. The Bland-Altman plot revealed that the majority of regions had errors within the  $2\sigma$  range, demonstrating excellent agreement between MALF and OpenMAP-T1. However, a few regions in both the ADNI3 and OASIS4 databases exhibited disagreements exceeding  $2\sigma$ . Figure 6C shows a weak correlation between the volumes of the regions and their Dice scores ( $R = 0.660$  in ADNI3,  $R = 0.707$  in OASIS4), despite most regions having a Dice score higher than 0.7. This implies that smaller regions tend to have greater discrepancies between the measurements from MALF and OpenMAP-T1. Additional results for other databases can be found in the Supplementary Material (Figure F, G and H).

We noted that certain anatomical labels were absent from the predicted parcellation map produced by OpenMAP-T1, specifically in the right rostral anterior cingulate white matter and the bilateral fimbria. A similar trend of omitting these small structures was observed with MALF. MALF results were as follows: 1.26 mm<sup>3</sup> with 924 of 929 instances for the right rostral anterior cingulate white matter; 6.37 mm<sup>3</sup> with 493 of 929 instances for the left fimbria; and 12.86 mm<sup>3</sup> with 136 of 929 instances for the right fimbria.

## Generalizability

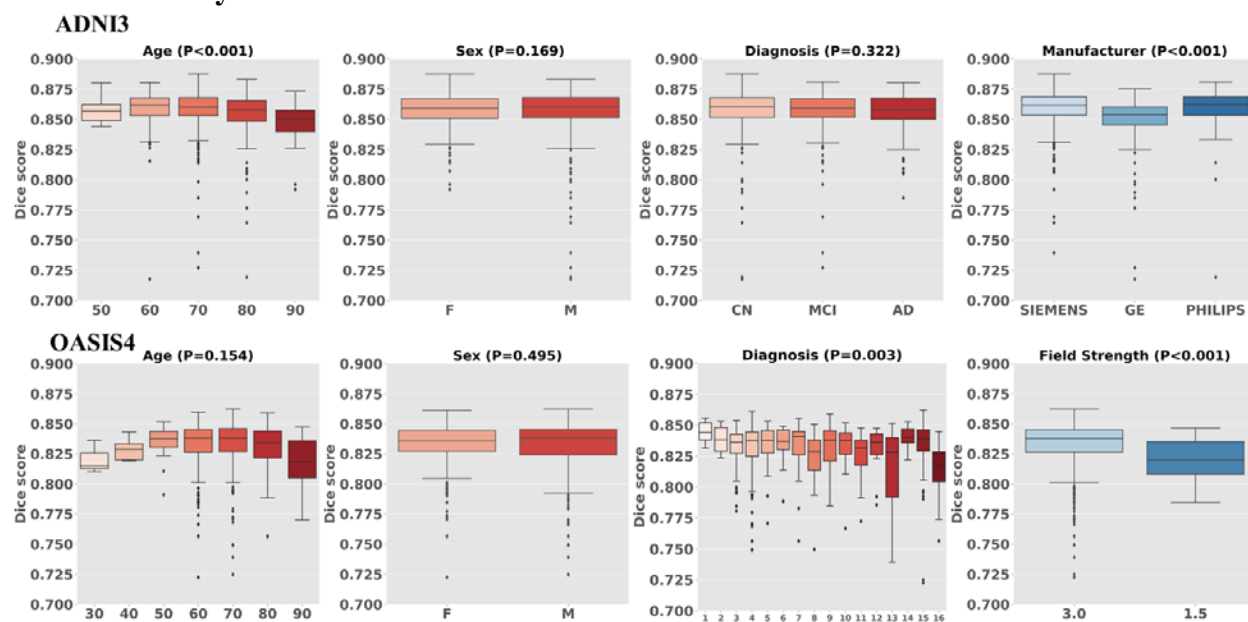


Figure 7. Boxplot of biological (age, sex, diagnosis) and technological effects (manufacturer, field strength) with Dice score. OASIS4 includes 16 diagnostic labels: 1: AD variant; 2: AD + non neurodegenerative; 3: AD / vascular; 4: alzheimer disease dementia; 5: Cognitively Normal (CN); 6: Dementia with Lewy Bodies (DLB); 7: early onset AD; 8: Frontotemporal Dementia (FTD); 9: Mild Cognitive Impairment (MCI); 10: mood / polypharmacy / sleep; 11: non-neurodegenerative neurologic disease; 12: other-miscellaneous; 13: other non-AD neurodegenerative disorder; 14: Primary Progressive Aphasia (PPA); 15: uncertain - AD possible; 16: Vascular Cognitive Impairment (VCI).

Figure 7 shows the Dice scores across biological (age, sex, and diagnosis) and technological (scanner manufacturer and field strength) categories, for the ADNI3 and OASIS4 datasets. The results from other databases are provided in the Supplementary Material (Table A). The red boxplots illustrate the influence of biological factors, while the blue boxplots represent the impact of technological factors. The Dice scores exceeded 0.8 in all conditions. Age had a significant effect in ADNI2, where the Dice score tended to decrease in individuals in their 90s. A similar trend was observed in OASIS4, although the effect was not statistically significant. No significant differences were noted based on sex in either database. Regarding the diagnosis, a significant effect was observed in OASIS4, where a diagnosis of VCI was associated with lower Dice scores compared to other diagnoses; however, in ADNI3, the diagnosis did not significantly impact Dice scores. Among the scanner manufacturers, GE systems showed lower Dice scores compared to those from Philips and Siemens. In terms of field strength, scanners operating at 1.5 T had lower Dice scores compared to those operating at 3T.

### Runtime

OpenMAP-T1 performed complete parcellation at 90 sec/case using a single GPU (RTX3090) and 10 min/case using a CPU (i9-10980XE). This result shows that OpenMAP-T1 is 40 times faster than MRICloud, which is one hour/case.

## 3.2. Comparison with FreeSurfer

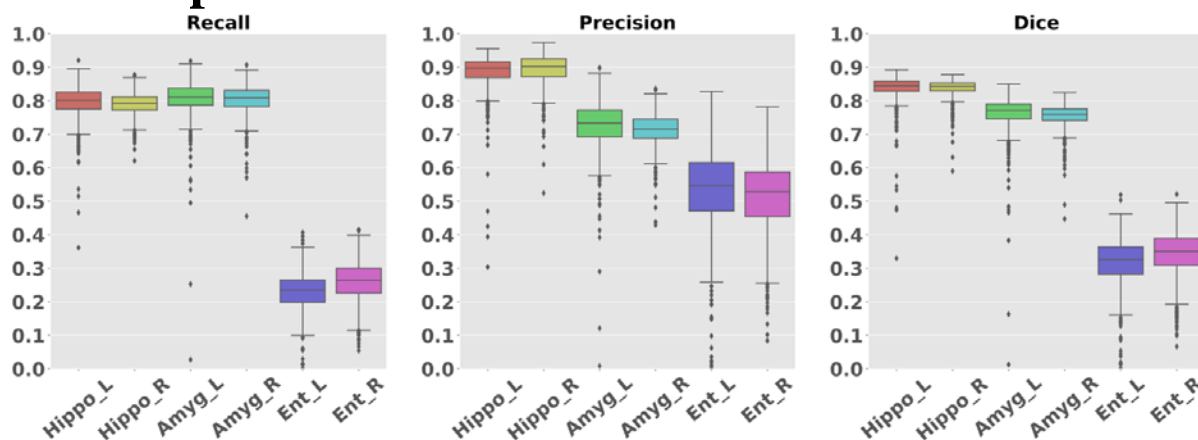


Figure 8. Boxplot of the Recall, Precision, and Dice scores in hippocampus, amygdala, and entorhinal regions.

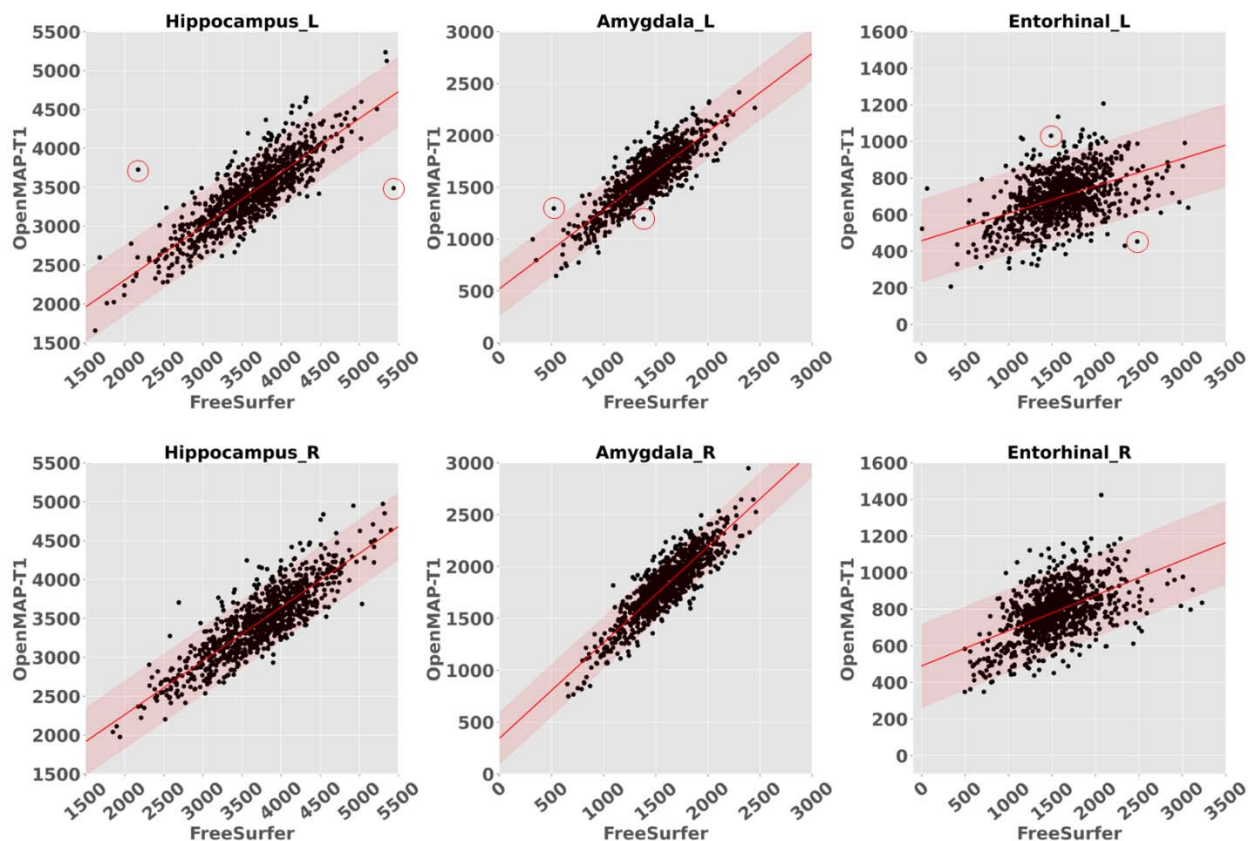


Figure 9. The correlations between the predicted volumes of the hippocampus, amygdala, and entorhinal cortex as obtained by OpenMAP-T1 and FreeSurfer. The upper row displays the results from the left side, while the lower row presents the results from the right side in ADNI3. The red lines represent the regression lines, while the transparent red areas show the range encompassing three standard deviations from these fitted regression lines. The red circles in the graph correspond to the representative images showcased in Figure 10.

Figure 8 shows the recall, precision, and Dice scores for the hippocampus, amygdala, and entorhinal cortex in the parcellation maps of OpenMAP-T1 and FreeSurfer, considering the results of FreeSurfer as the ground truth. Figure 9 compares the predicted volumes in the hippocampus, amygdala, and entorhinal cortex between OpenMAP-T1 and FreeSurfer. In the hippocampus, the recall, precision, and Dice scores were all high. This result indicated that the definition of the hippocampus boundary was nearly identical in OpenMAP-T1 and FreeSurfer, and both methods were equally accurate in identifying the hippocampus. As shown in Figure 9, the hippocampal volume measurements obtained by both methods correlated well. In the amygdala, although the recall was equivalent to that of the hippocampus, the precision and Dice scores were lower. This suggests the existence of systematic bias due to methodological differences in defining the amygdala region; the amygdala region defined by FreeSurfer was smaller than that defined by OpenMAP-T1, which includes the cortical amygdala not included in the FreeSurfer definition. As demonstrated in Figure 9, although the volume measurements of both methods correlated well, FreeSurfer consistently underestimated the amygdala volume compared to OpenMAP-T1. Conversely, FreeSurfer defined the entorhinal cortex area as larger than OpenMAP-T1 and often included the adjacent dura matter within the entorhinal cortex

region (see Figure 10). Therefore, while precision was relatively preserved, the recall and Dice scores were lower, and the correlation of volume measurements between the two methods was weaker for the entorhinal cortex compared to the hippocampus and amygdala.

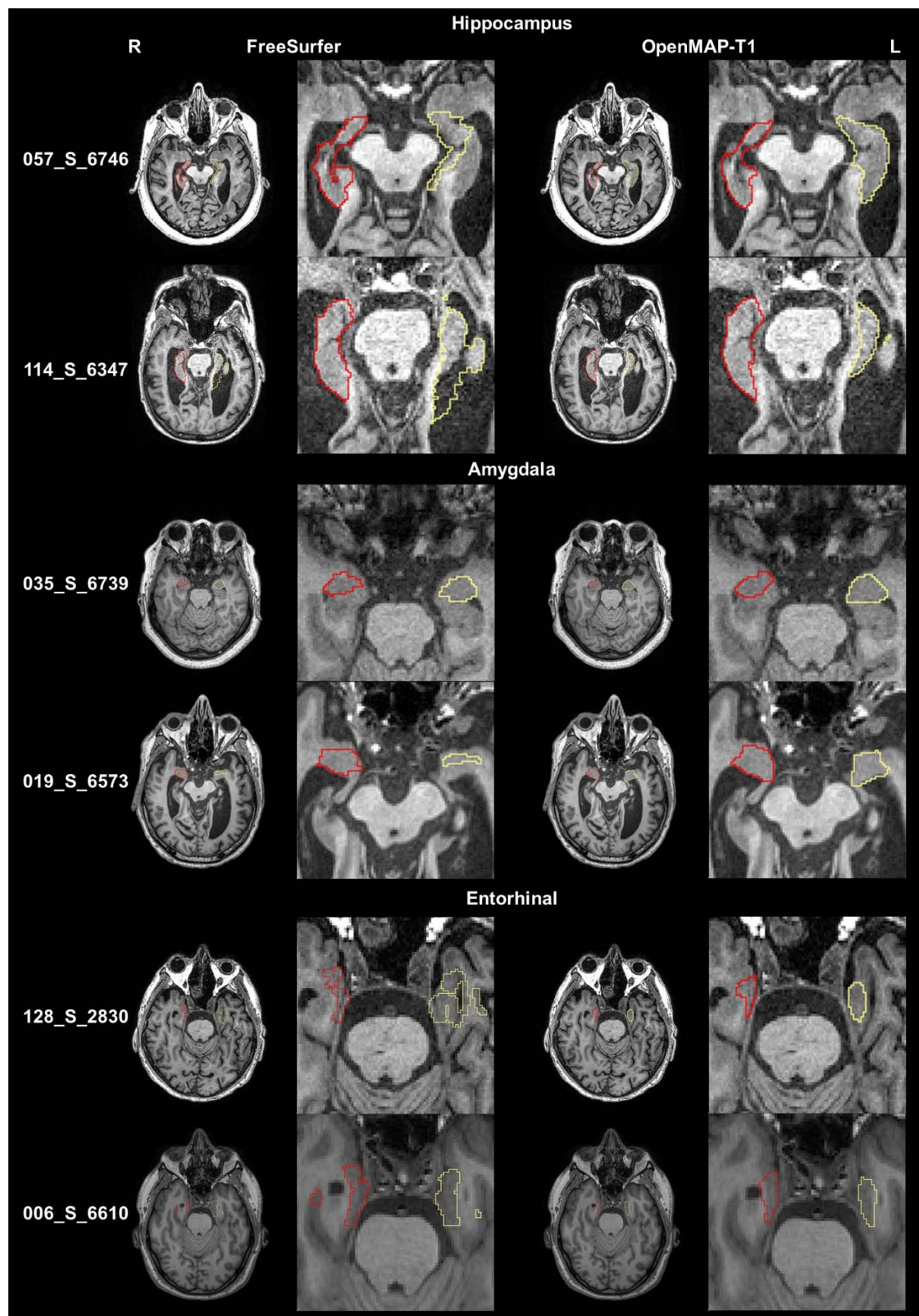


Figure 10. The parcellation maps from OpenMAP-T1 and FreeSurfer overlaid on the MPRAGE images that correspond to the red circles in Figure 9 are demonstrated. The leftmost column shows the study IDs from the ADNI3 dataset. Axial slices along with magnified images of the hippocampus, amygdala, and entorhinal cortex are presented. The red borderlines indicate the regions on the right side, while the yellow borderlines mark the regions on the left side. These images adhere to the radiological convention, where the left side of the brain is shown on the right side of the image.

Figure 10 displays representative images linked to the outliers in Figure 9. The primary reasons for the low Dice scores were generally due to mislabeling by FreeSurfer, differences in anatomical definitions between OpenMAP-T1 and FreeSurfer, or a combination of both. For instance, in image 057\_S\_6746, FreeSurfer incorrectly labeled the left hippocampus. In image 114\_S\_6347, FreeSurfer erroneously included a part of the lateral ventricle in the left hippocampus ROI. The boundary of the amygdala was delineated smaller by FreeSurfer than defined by OpenMAP-T1 in images 035\_S\_6739 and 019\_S\_6573, which is attributable to the differing anatomical definitions between the two. Furthermore, FreeSurfer typically incorporated the perirhinal cortex and the dura mater adjacent to the entorhinal cortex into the entorhinal ROI. In contrast, the definition of the entorhinal cortex in OpenMAP-T1 does not include these areas, as evident in images 128\_S\_2830 and 006\_S\_6610.

### 3.3. Biological Evaluation

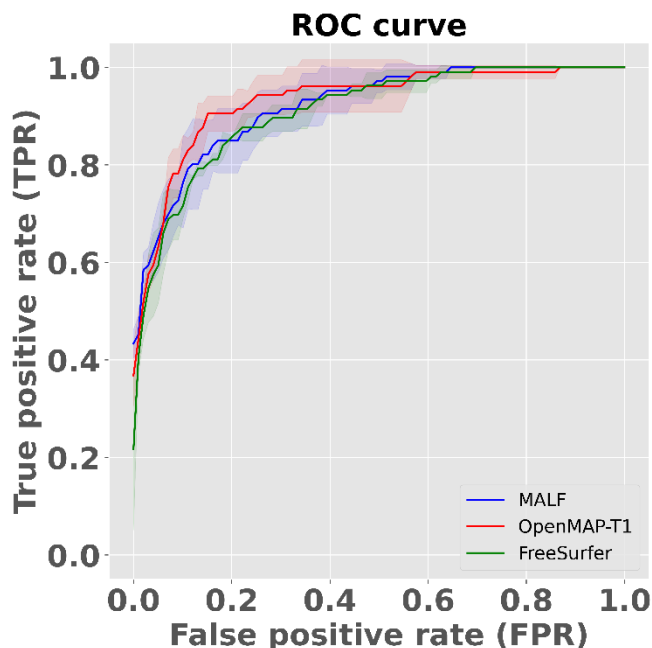


Figure 11. The Receiver Operatorating Characteristic (ROC) curve for distinguishing between AD and CN based on predicted volumes using the LASSO model. The blue line represents the ROC curve for MALF, the red line for OpenMAP-T1, and the green line for FreeSurfer. The shaded areas around each line indicate the standard deviation.

AUC values for the ROC curves were 0.920 for MALF, 0.930 for OpenMAP-T1, and 0.908 for FreeSurfer. There were no significant differences between these AUC values. The p-values

derived from the DeLong test were 0.618 when comparing MALF and OpenMAP-T1, and 0.271 when comparing OpenMAP-T1 and FreeSurfer.

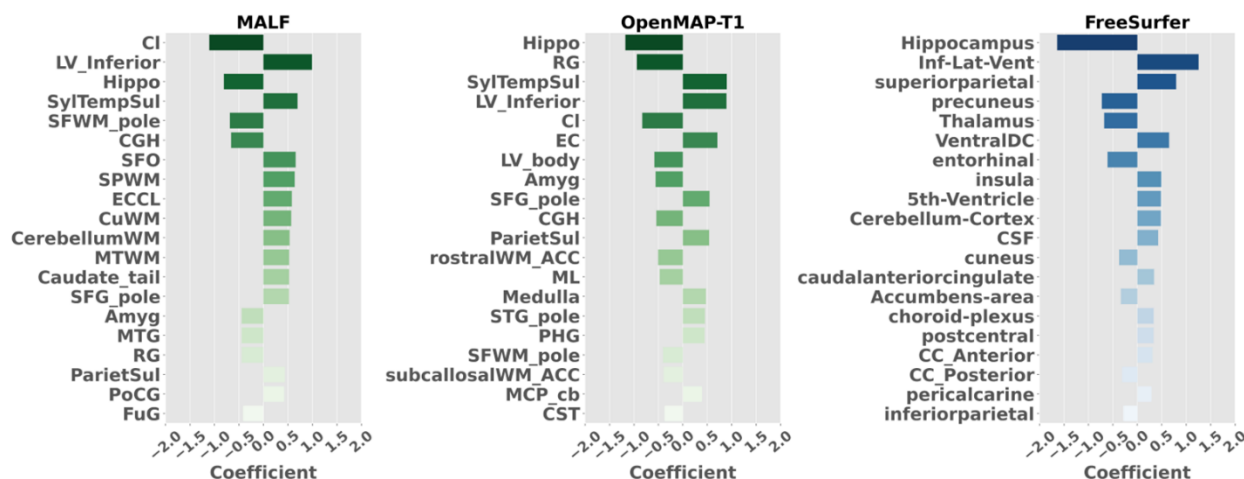


Figure 12. The 20 anatomical regions that exhibited the highest correlation coefficients as determined by the trained LASSO model.

Among the top 20 anatomical regions with the highest correlation coefficients derived from the trained LASSO model, nine structures were common between MALF and OpenMAP-T1 (Figure 11). Of these, six structures – namely the hippocampus, amygdala, inferior horn and body of the lateral ventricle, Sylvian fissure, and the hippocampal part of the cingulum bundle – are known to be associated with AD pathologies [65-68], indicating the appropriateness of the LASSO model.

## 4. Discussion

We have developed and released a deep-learning model, called OpenMAP-T1, on Git-Hub, for the segmentation and parcellation of brain 3D T1-weighted MRI images, based on their anatomical structures. The performance of the model was evaluated using metrics such as recall, precision, Dice, and correlation based on comparisons between the OpenMAP-T1 and the established MALF algorithm. The results demonstrated that the parcellation outcomes were generally equivalent to the MALF method. Notably, the processing time was significantly reduced to less than 90 seconds per image, compared to the several hours required by the existing MALF method.

We introduced a multi-processing phase to create a parcellation model, which is robust against diverse imaging environments. In MRI parcellation using deep-learning, performance is often affected by differences in the imaging environment, particularly the defacing algorithm, between training and evaluation datasets [69]. To reduce the impact of irrelevant areas on whole-brain parcellation, we incorporated cropping and skull-stripping phases. Furthermore, the whole brain was parcellated into 141 regions combining left and right labels, inspired by the approach used in FastSurfer [44]. While FastSurfer combines the left and right labels using only the sagittal cross-section, OpenMAP-T1 can combine the left and right labels in all the cross-sections. Consequently, we could reduce the number of class (i.e., region labels) and increase the size of each region, which resulted in fast and accurate parcellation.

There is the potential to further enhance the processing speed of OpenMAP-T1. For instance, reducing the image matrix size could decrease the input size for the PNet. This reduction can be achieved by repositioning the center of gravity of the brain post skull-stripping, and then trimming areas outside the brain. We anticipate periodic updates to OpenMAP-T1, focusing on optimizing processing strategies and incorporating new features into the algorithms.

In recent years, the MPRAGE sequence with 3T scanners has been often used for anatomical MRI scans for brain research [70]. However, available open brain MRI databases contain legacy images scanned with MRI scanners from various vendors, models, and magnetic field strengths. These databases also include images scanned with the MPRAGE and other sequences, such as the SPGR sequence. The accuracy of brain parcellation was affected by variations in scanner types, magnetic field strengths, and scan protocols [71, 72]. Thus, automated brain MRI parcellation methods should be robust to these variations. Furthermore, it has been demonstrated that facial appearance can be reconstructed from a whole-head MRI [73]. In terms of a privacy protection perspective, some MRI databases [44] apply a defacing algorithm to prevent facial reconstruction. The ability of automated brain parcellation methods to handle such defaced MRIs is crucial in the era of open science and data sharing. Our results showed that the parcellation maps generated by MALF and OpenMAP-T1 are substantially similar (average Dice score  $> 0.8$ , except for LBPA40 database that collected SPGR images) regardless of the scanner vendor, magnetic field strength, scan protocol, or the presence of defacing. However, we found that Dice scores were significantly lower in SPGR images than those in MPRAGE images, from 1.5T to 3T scanners, as well as the Dice scores in GE scanners, which were significantly lower compared to those in Philips or Siemens.

We identified three major reasons that MALF and OpenMAP-T1 showed disagreement (Dice score  $< 0.8$ ). MALF tended to mislabel images with noticeable intensity inhomogeneity even after correction with the N4 algorithm. For instance, images scanned with 3D-SPGR sequences or 1.5T scanners resulted in blurring contrasts between the white matter and gray matter compared to MPRAGE or 3T scanners, or images that had undergone defacing resulted in low Dice scores as well. These low Dice scores were not caused by mislabeling by OpenMAP-T1, but rather, by MALF. MALF uses whole-head MPRAGE images scanned with 3T scanners as training data and employs image transformation using intensity information as a cost function [38]. Therefore, MALF is vulnerable to intensity inhomogeneity, and its parcellation accuracy might be affected by differences in scanner magnetic field strength, scan protocols, and defacing. In contrast, OpenMAP-T1, which uses deep-learning with data augmentation, was more robust than MALF against variations in image intensity inhomogeneity and scanning parameters.

Images with notable intensity inhomogeneity, even after intensity correction, were often scanned in a head-extended position. Such position is often seen in older participants with neurological conditions [74, 75], leading to a decrease in image intensity in areas distant from the physical center of the MRI scanner, such as the frontal pole or the posteroinferior occipital lobe and cerebellum. The robustness of OpenMAP-T1 for the abnormal head position seems advantageous for the analysis of disease images. Moreover, artifacts that introduce high-signal pixels potentially hinder successful intensity correction. The results with OpenMAP-T1 indicated its robustness against such artifacts.

Defacing may become a standard procedure when sharing brain MRI images [76-78]. However, many brain parcellation methods have not been tested on images that have undergone defacing. Implementing a refacing process, which adds artificial facial information after defacing, is being considered to avoid changes in parcellation accuracy due to defacing [73]. Meanwhile, OpenMAP-T1 has demonstrated its capability to parcellate images from the NFBS and OASIS1 databases, which have used different defacing methods, indicating its adaptability for future mainstream databases of defaced images.

From the perspective of precision medicine, a significant topic has been whether insights gained from basic research and clinical trials can be adapted to actual clinical data. Research often involves strict inclusion and exclusion criteria, targeting specific individuals, inevitably leading to selection bias [79-81]. Therefore, using real-world data is essential when considering the applicability to clinical data. For developing automated brain MRI parcellation methods, assessing their accuracy using brain images obtained through clinical practice is crucial. To evaluate the applicability of OpenMAP-T1 in real clinical settings, we used real-world data from OASIS4. The average Dice score exceeded 0.8 in OASIS4, suggesting potential adaptability to images obtained through clinical practice.

When testing research data such as ADNI, the Dice score was unaffected by sex or diagnostic category, including cognitively normal (CN), MCI, and AD. However, in the real-world data of OASIS4, while the Dice score was not influenced by age or sex, it was affected by clinical diagnosis. Average Dice scores of groups with "other non-AD neurodegenerative disorders" and "vascular cognitive impairment" tended to be lower than other diagnostic groups, although they still demonstrated average Dice scores above 0.8. Many images with Dice scores below 0.8 were due to mislabeling by MALF in the presence of lesions, but, in patients with large arachnoid cysts at the posterior area, both MALF and OpenMAP-T1 mislabeled the lesion. This result suggests that OpenMAP-T1 may mislabel images containing large lesions, likely due to a lack of such images in its training data, indicating potential areas for future improvement.

FreeSurfer is one of the most commonly used softwares for brain MRI parcellation [82, 83]. FreeSurfer is suitable for comprehensive analysis of the cerebral cortex with its ability to measure the thickness of the cerebral cortex. However, OpenMAP-T1 can parcellate both gray and white matter areas, thus offering the advantage of simultaneous analysis of the cortex and white matter. Since the definitions of the brain regions employed by both softwares differ, and their intended uses are different, it is difficult to compare the parcellation performance of the two. Therefore, their performance was compared in a task that separates brain MRIs of AD and CN individuals. In AD research, the amygdala, entorhinal cortex, and hippocampus volumes are often used as neurodegeneration markers. When comparing these volumes measured by FreeSurfer and OpenMAP-T1, a good correlation was found in these regions. Furthermore, the brain regions that played a significant role in separating AD and CN, obtained from the LASSO model, were similar, and there was no difference between FreeSurfer and OpenMAP-T1 in separation performance for AD and CN as analyzed by ROC analysis. Therefore, the choice between FreeSurfer and OpenMAP-T1 should not be based on which has more accurate parcellation, but should be selected according to the research objectives and the anatomical structures of interest.

## 5. Limitations

OpenMAP-T1 has several limitations. As with any parcellation method, in small ROIs, precision, recall, and Dice scores can be significantly reduced by minor boundary differences, making it challenging to evaluate the accuracy of parcellation itself. Furthermore, whether parcellation can be accurately performed on images containing various lesions, such as large cerebral infarcts, brain hemorrhages, or brain tumors, is a topic for future investigation. Using real clinical images as training data for clinical applications might be necessary. Also, while the analyzed images in this study were high-resolution 3D images, many clinical images use 2D imaging methods with a thickness of 5mm or more. Whether OpenMAP-T1 can be applied to such thick-slice 2D images is also a subject for future study.

## 6. Conclusion

We developed OpenMAP-T1, a model based on deep-learning for segmentation and parcellation of brain T1-weighted MRI images according to anatomical structures, and evaluated its accuracy across eight test datasets. OpenMAP-T1 could accurately perform parcellation regardless of technological variations such as the scanner vendor, magnetic field strength, defacing, imaging parameters, defacing, and biological variations, including differences in sex, age, and disease. It could also parcellate images with postural changes in the head or images with intensity inhomogeneity. In a task using machine-learning to differentiate between AD and CN based on parcellation maps, the discriminative ability of OpenMAP-T1 was found to be equivalent to that obtained using MALF or FreeSurfer. However, OpenMAP-T1 was able to process images much faster compared to the traditional MALF method and FreeSurfer. These results suggest that OpenMAP-T1 is a promising method for high-speed image parcellation that can accommodate various types of lesions. OpenMAP-T1 is available on our GitHub (URL: <https://github.com/OishiLab/OpenMAP>).

## 7. Acknowledgment

The MRI data collection and sharing for this project was funded by the Alzheimer's Disease Neuroimaging Initiative (ADNI) (National Institutes of Health Grant U01 AG024904) and DOD ADNI (Department of Defense award number W81XWH-12-2-0012). ADNI is funded by the National Institute on Aging, the National Institute of Biomedical Imaging and Bioengineering, and through generous contributions from the following: AbbVie, Alzheimer's Association; Alzheimer's Drug Discovery Foundation; Araclon Biotech; BioClinica, Inc.; Biogen; Bristol-Myers Squibb Company; CereSpir, Inc.; Cogstate; Eisai Inc.; Elan Pharmaceuticals, Inc.; Eli Lilly and Company; EuroImmun; F. Hoffmann-La Roche Ltd. and its affiliated company Genentech, Inc.; Fujirebio; GE Healthcare; IXICO Ltd.; Janssen Alzheimer Immunotherapy Research & Development, LLC.; Johnson & Johnson Pharmaceutical Research & Development LLC.; Lumosity; Lundbeck; Merck & Co., Inc.; Meso Scale Diagnostics, LLC.; NeuroRx Research; Neurotrack Technologies; Novartis Pharmaceuticals Corporation; Pfizer Inc.; Piramal Imaging; Servier; Takeda Pharmaceutical Company; and Transition Therapeutics. The Canadian Institutes of Health Research is providing funds to support ADNI clinical sites in Canada. Private sector contributions are facilitated by the Foundation for the National Institutes of Health

([www.fnih.org](http://www.fnih.org)). The grantee organization is the Northern California Institute for Research and Education, and the study is coordinated by the Alzheimer's Therapeutic Research Institute at the University of Southern California. ADNI data are disseminated by the Laboratory for Neuro Imaging at the University of Southern California.

Data were provided by OASIS1/4: Cross-Sectional: Principal Investigators: D. Marcus, R. Buckner, J. Csernansky, J. Morris; P50 AG05681, P01 AG03991, P01 AG026276, R01 AG021910, P20 MH071616, U24 RR021382 and Clinical Cohort: Principal Investigators: T. Benzinger, L. Koenig, P. LaMontagne.

We would like to thank Jill Chotiyanonta for providing feedback on the accuracy of brain MRI parcellation results obtained from MRICloud, and Mary McAllister for her assistance with editing the English.

## References

- [1] Aljabar P, Heckemann RA, Hammers A, Hajnal JV, Rueckert D. Multi-atlas based segmentation of brain images: atlas selection and its effect on accuracy. *Neuroimage*. 2009;46:726-38.
- [2] Blesa M, Serag A, Wilkinson AG, Anblagan D, Telford EJ, Pataky R, Sparrow SA, Macnaught G, Semple SI, Bastin ME, Boardman JP. Parcellation of the Healthy Neonatal Brain into 107 Regions Using Atlas Propagation through Intermediate Time Points in Childhood. *Frontiers in neuroscience*. 2016;10:220.
- [3] Chapman T, Matesan M, Weinberger E, Bulas DI. Digital atlas of fetal brain MRI. *Pediatric radiology*. 2010;40:153-62.
- [4] Deshpande R, Chang L, Oishi K. Construction and application of human neonatal DTI atlases. *Frontiers in neuroanatomy*. 2015;9:138.
- [5] Fan L, Li H, Zhuo J, Zhang Y, Wang J, Chen L, Yang Z, Chu C, Xie S, Laird AR, Fox PT, Eickhoff SB, Yu C, Jiang T. The Human Brainnetome Atlas: A New Brain Atlas Based on Connectional Architecture. *Cereb Cortex*. 2016;26:3508-26.
- [6] Gholipour A, Limperopoulos C, Clancy S, Clouchoux C, Akhondi-Asl A, Estroff JA, Warfield SK. Construction of a deformable spatiotemporal MRI atlas of the fetal brain: evaluation of similarity metrics and deformation models. *Med Image Comput Comput Assist Interv*. 2014;17:292-9.
- [7] Habas PA, Kim K, Rousseau F, Glenn OA, Barkovich AJ, Studholme C. Atlas-based segmentation of the germinal matrix from in utero clinical MRI of the fetal brain. *Med Image Comput Comput Assist Interv*. 2008;11:351-8.
- [8] Mori S, Oishi K, Faria AV, Miller MI. Atlas-based neuroinformatics via MRI: harnessing information from past clinical cases and quantitative image analysis for patient care. *Annual review of biomedical engineering*. 2013;15:71-92.
- [9] Oishi K, Chang L, Huang H. Baby brain atlases. *Neuroimage*. 2019;185:865-80.
- [10] Oishi K, Faria A, Jiang H, Li X, Akhter K, Zhang J, Hsu JT, Miller MI, van Zijl PC, Albert M, Lyketsos CG, Woods R, Toga AW, Pike GB, Rosa-Neto P, Evans A, Mazziotta J, Mori S. Atlas-based whole brain white matter analysis using large deformation diffeomorphic metric mapping: application to normal elderly and Alzheimer's disease participants. *Neuroimage*. 2009;46:486-99.
- [11] Oishi K, Faria AV, van Zijl PCM, Mori S. *MRI Atlas of Human White Matter*: Elsevier Science; 2010.
- [12] Oishi K, Mori S, Donohue PK, Ernst T, Anderson L, Buchthal S, Faria A, Jiang H, Li X, Miller MI, van Zijl PC, Chang L. Multi-contrast human neonatal brain atlas: application to normal neonate development analysis. *Neuroimage*. 2011;56:8-20.
- [13] Oishi K, Zilles K, Amunts K, Faria A, Jiang H, Li X, Akhter K, Hua K, Woods R, Toga AW, Pike GB, Rosa-Neto P, Evans A, Zhang J, Huang H, Miller MI, van Zijl PC, Mazziotta J, Mori S. Human brain white matter atlas: identification and assignment of common anatomical structures in superficial white matter. *Neuroimage*. 2008;43:447-57.
- [14] Otsuka Y, Chang L, Kawasaki Y, Wu D, Ceritoglu C, Oishi K, Ernst T, Miller M, Mori S, Oishi K. A Multi-Atlas Label Fusion Tool for Neonatal Brain MRI Parcellation and Quantification. *J Neuroimaging*. 2019.

- [15] Qin YY, Hsu JT, Yoshida S, Faria AV, Oishi K, Unschuld PG, Redgrave GW, Ying HS, Ross CA, Van Zijl PCM, Hillis AE, Albert MS, Lyketsos CG, Miller MI, Mori S, Oishi K. Gross feature recognition of Anatomical Images based on Atlas grid (GAIA): Using the Degree of Local Atlas-Image Segmentation Disagreement to Capture the Features of Anatomic Brain MRI. *NeuroImage: Clinical*. 2013;In Press.
- [16] Tzourio-Mazoyer N, Landeau B, Papathanassiou D, Crivello F, Etard O, Delcroix N, Mazoyer B, Joliot M. Automated anatomical labeling of activations in SPM using a macroscopic anatomical parcellation of the MNI MRI single-subject brain. *Neuroimage*. 2002;15:273-89.
- [17] Maldjian JA, Laurienti PJ, Kraft RA, Burdette JH. An automated method for neuroanatomic and cytoarchitectonic atlas-based interrogation of fMRI data sets. *Neuroimage*. 2003;19:1233-9.
- [18] Klein A, Tourville J. 101 labeled brain images and a consistent human cortical labeling protocol. *Frontiers in neuroscience*. 2012;6:171.
- [19] Desikan RS, Segonne F, Fischl B, Quinn BT, Dickerson BC, Blacker D, Buckner RL, Dale AM, Maguire RP, Hyman BT, Albert MS, Killiany RJ. An automated labeling system for subdividing the human cerebral cortex on MRI scans into gyral based regions of interest. *Neuroimage*. 2006;31:968-80.
- [20] Destrieux C, Fischl B, Dale A, Halgren E. Automatic parcellation of human cortical gyri and sulci using standard anatomical nomenclature. *Neuroimage*. 2010;53:1-15.
- [21] Hansen JY, Shafiei G, Markello RD, Smart K, Cox SML, Norgaard M, Beliveau V, Wu Y, Gallezot JD, Aumont E, Servaes S, Scala SG, DuBois JM, Wainstein G, Bezgin G, Funck T, Schmitz TW, Spreng RN, Galovic M, Koepp MJ, Duncan JS, Coles JP, Fryer TD, Aigbirhio FI, McGinnity CJ, Hammers A, Soucy JP, Baillet S, Guimond S, Hietala J, Bedard MA, Leyton M, Kobayashi E, Rosa-Neto P, Ganz M, Knudsen GM, Palomero-Gallagher N, Shine JM, Carson RE, Tuominen L, Dagher A, Masic B. Mapping neurotransmitter systems to the structural and functional organization of the human neocortex. *Nat Neurosci*. 2022;25:1569-81.
- [22] Beliveau V, Ganz M, Feng L, Ozenne B, Hojgaard L, Fisher PM, Svarer C, Greve DN, Knudsen GM. A High-Resolution In Vivo Atlas of the Human Brain's Serotonin System. *J Neurosci*. 2017;37:120-8.
- [23] Liu CF, Hsu J, Xu X, Kim G, Sheppard SM, Meier EL, Miller MI, Hillis AE, Faria AV. Digital 3D Brain MRI Arterial Territories Atlas. *Sci Data*. 2023;10:74.
- [24] Gordon EM, Laumann TO, Adeyemo B, Huckins JF, Kelley WM, Petersen SE. Generation and Evaluation of a Cortical Area Parcellation from Resting-State Correlations. *Cereb Cortex*. 2016;26:288-303.
- [25] Doucet GE, Lee WH, Frangou S. Evaluation of the spatial variability in the major resting-state networks across human brain functional atlases. *Hum Brain Mapp*. 2019;40:4577-87.
- [26] Yan X, Kong R, Xue A, Yang Q, Orban C, An L, Holmes AJ, Qian X, Chen J, Zuo XN, Zhou JH, Fortier MV, Tan AP, Gluckman P, Chong YS, Meaney MJ, Bzdok D, Eickhoff SB, Yeo BTT. Homotopic local-global parcellation of the human cerebral cortex from resting-state functional connectivity. *Neuroimage*. 2023;273:120010.
- [27] Schaefer A, Kong R, Gordon EM, Laumann TO, Zuo XN, Holmes AJ, Eickhoff SB, Yeo BTT. Local-Global Parcellation of the Human Cerebral Cortex from Intrinsic Functional Connectivity MRI. *Cereb Cortex*. 2018;28:3095-114.

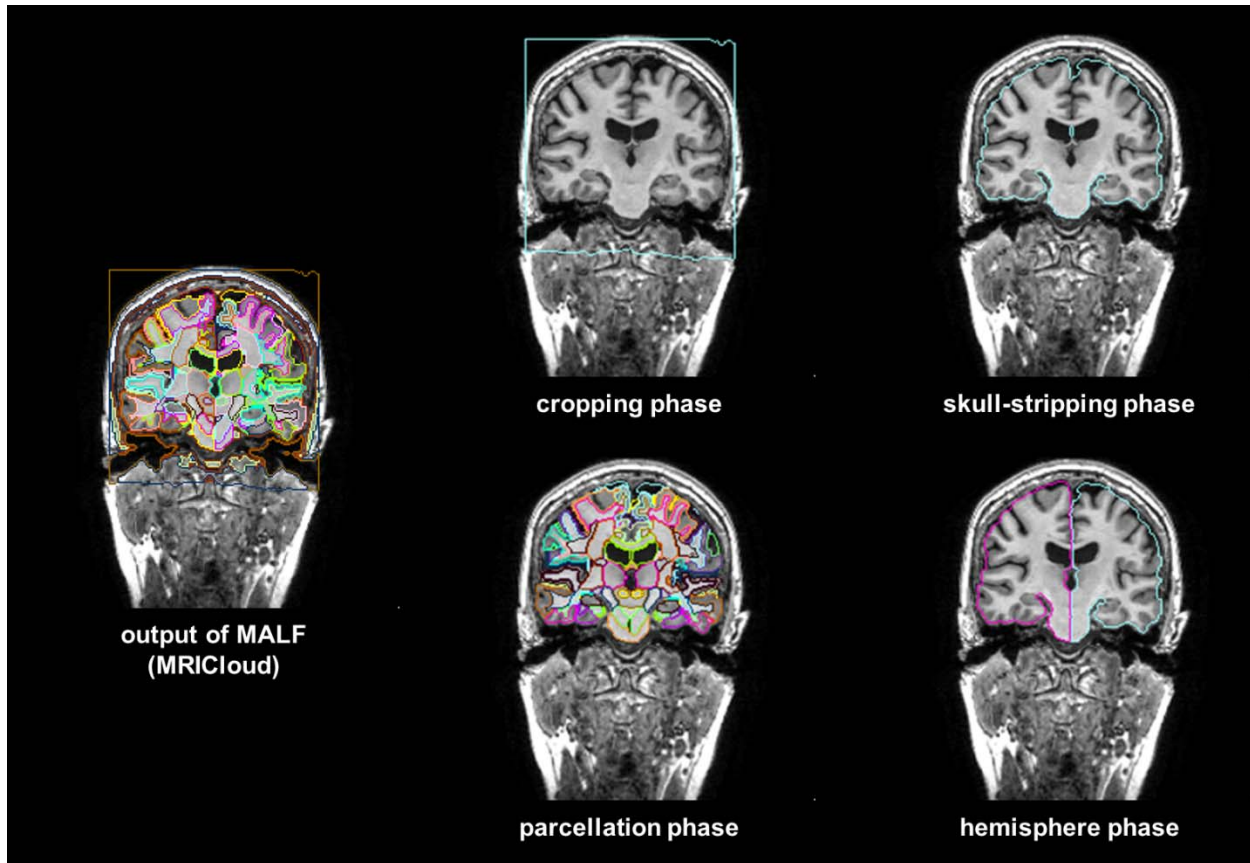
- [28] Joliot M, Jobard G, Naveau M, Delcroix N, Petit L, Zago L, Crivello F, Mellet E, Mazoyer B, Tzourio-Mazoyer N. AICHA: An atlas of intrinsic connectivity of homotopic areas. *Journal of neuroscience methods*. 2015;254:46-59.
- [29] Yeo BT, Krienen FM, Sepulcre J, Sabuncu MR, Lashkari D, Hollinshead M, Roffman JL, Smoller JW, Zollei L, Polimeni JR, Fischl B, Liu H, Buckner RL. The organization of the human cerebral cortex estimated by intrinsic functional connectivity. *J Neurophysiol*. 2011;106:1125-65.
- [30] Djamanakova A, Faria AV, Hsu J, Ceritoglu C, Oishi K, Miller MI, Hillis AE, Mori S. Diffeomorphic brain mapping based on T1-weighted images: improvement of registration accuracy by multichannel mapping. *J Magn Reson Imaging*. 2013;37:76-84.
- [31] Dolz J, Massotier L, Vermandel M. Segmentation algorithms of subcortical brain structures on MRI for radiotherapy and radiosurgery: A survey. *Irbm*. 2015;36:200-12.
- [32] Sabuncu MR, Yeo BT, Van Leemput K, Fischl B, Golland P. A generative model for image segmentation based on label fusion. *IEEE Trans Med Imaging*. 2010;29:1714-29.
- [33] Wang H, Suh JW, Das SR, Pluta JB, Craige C, Yushkevich PA. Multi-Atlas Segmentation with Joint Label Fusion. *IEEE Trans Pattern Anal Mach Intell*. 2013;35:611-23.
- [34] Collins DL, Pruessner JC. Towards accurate, automatic segmentation of the hippocampus and amygdala from MRI by augmenting ANIMAL with a template library and label fusion. *Neuroimage*. 2010;52:1355-66.
- [35] Asman AJ, Dagley AS, Landman BA. Statistical label fusion with hierarchical performance models. *Proc SPIE Int Soc Opt Eng*. 2014;9034:90341E.
- [36] Wu G, Wang Q, Zhang D, Nie F, Huang H, Shen D. A generative probability model of joint label fusion for multi-atlas based brain segmentation. *Medical image analysis*. 2014;18:881-90.
- [37] Asman AJ, Huo Y, Plassard AJ, Landman BA. Multi-atlas learner fusion: An efficient segmentation approach for large-scale data. *Med Image Anal*. 2015;26:82-91.
- [38] Mori S, Wu D, Li Y, Kolasny A, Vaillant MA, Faria AV, Oishi K, Miller MI. MRICloud: Delivering High-Throughput MRI Neuroinformatics as Cloud-Based Software as a Service. *Computing in Science & Engineering*. 2016;18:21-35.
- [39] Wu G, Kim M, Sanroma G, Wang Q, Munsell BC, Shen D, Alzheimer's Disease Neuroimaging I. Hierarchical multi-atlas label fusion with multi-scale feature representation and label-specific patch partition. *Neuroimage*. 2015;106:34-46.
- [40] Li W, Wang G, Fidon L, Ourselin S, Cardoso MJ, Vercauteren T. On the Compactness, Efficiency, and Representation of 3D Convolutional Networks: Brain Parcellation as a Pretext Task. 2017:arXiv:1707.01992.
- [41] Rajchl M, Pawlowski N, Rueckert D, Matthews PM, Glocker B. NeuroNet: Fast and Robust Reproduction of Multiple Brain Image Segmentation Pipelines. 2018:arXiv:1806.04224.
- [42] Huo Y, Xu Z, Xiong Y, Aboud K, Parvathaneni P, Bao S, Bermudez C, Resnick SM, Cutting LE, Landman BA. 3D whole brain segmentation using spatially localized atlas network tiles. *Neuroimage*. 2019;194:105-19.
- [43] Coupe P, Mansencal B, Clement M, Giraud R, Denis de Senneville B, Ta VT, Lepetit V, Manjon JV. AssemblyNet: A large ensemble of CNNs for 3D whole brain MRI segmentation. *Neuroimage*. 2020;219:117026.
- [44] Henschel L, Conjeti S, Estrada S, Diers K, Fischl B, Reuter M. FastSurfer - A fast and accurate deep learning based neuroimaging pipeline. *Neuroimage*. 2020;219:117012.

- [45] Thyreau B, Taki Y. Learning a cortical parcellation of the brain robust to the MRI segmentation with convolutional neural networks. *Med Image Anal.* 2020;61:101639.
- [46] Lim EC, Choi US, Choi KY, Lee JJ, Sung YW, Ogawa S, Kim BC, Lee KH, Gim J, Alzheimer's Disease Neuroimaging I. DeepParcellation: A novel deep learning method for robust brain magnetic resonance imaging parcellation in older East Asians. *Front Aging Neurosci.* 2022;14:1027857.
- [47] Yu X, Yang Q, Zhou Y, Cai LY, Gao R, Lee HH, Li T, Bao S, Xu Z, Lasko TA, Abramson RG, Zhang Z, Huo Y, Landman BA, Tang Y. UNesT: Local spatial representation learning with hierarchical transformer for efficient medical segmentation. *Med Image Anal.* 2023;90:102939.
- [48] Fischl B. FreeSurfer. *Neuroimage.* 2012;62:774-81.
- [49] Weiner MW, Aisen PS, Jack CR, Jr., Jagust WJ, Trojanowski JQ, Shaw L, Saykin AJ, Morris JC, Cairns N, Beckett LA, Toga A, Green R, Walter S, Soares H, Snyder P, Siemers E, Potter W, Cole PE, Schmidt M, Alzheimer's Disease Neuroimaging I. The Alzheimer's disease neuroimaging initiative: progress report and future plans. *Alzheimers Dement.* 2010;6:202-11 e7.
- [50] Ellis KA, Bush AI, Darby D, De Fazio D, Foster J, Hudson P, Lautenschlager NT, Lenzo N, Martins RN, Maruff P, Masters C, Milner A, Pike K, Rowe C, Savage G, Szoeka C, Taddei K, Villemagne V, Woodward M, Ames D, Group AR. The Australian Imaging, Biomarkers and Lifestyle (AIBL) study of aging: methodology and baseline characteristics of 1112 individuals recruited for a longitudinal study of Alzheimer's disease. *Int Psychogeriatr.* 2009;21:672-87.
- [51] Ellis KA, Szoeka C, Bush AI, Darby D, Graham PL, Lautenschlager NT, Macaulay SL, Martins RN, Maruff P, Masters CL, McBride SJ, Pike KE, Rainey-Smith SR, Rembach A, Robertson J, Rowe CC, Savage G, Villemagne VL, Woodward M, Wilson W, Zhang P, Ames D, Group AR. Rates of diagnostic transition and cognitive change at 18-month follow-up among 1,112 participants in the Australian Imaging, Biomarkers and Lifestyle Flagship Study of Ageing (AIBL). *Int Psychogeriatr.* 2014;26:543-54.
- [52] Souza R, Lucena O, Garrafa J, Gobbi D, Saluzzi M, Appenzeller S, Rittner L, Frayne R, Lotufo R. An open, multi-vendor, multi-field-strength brain MR dataset and analysis of publicly available skull stripping methods agreement. *Neuroimage.* 2018;170:482-94.
- [53] Shattuck DW, Mirza M, Adisetiyo V, Hojatkashani C, Salamon G, Narr KL, Poldrack RA, Bilder RM, Toga AW. Construction of a 3D probabilistic atlas of human cortical structures. *Neuroimage.* 2008;39:1064-80.
- [54] Puccio B, Pooley JP, Pellman JS, Taverna EC, Craddock RC. The preprocessed connectomes project repository of manually corrected skull-stripped T1-weighted anatomical MRI data. *Gigascience.* 2016;5:45.
- [55] Marcus DS, Wang TH, Parker J, Csernansky JG, Morris JC, Buckner RL. Open Access Series of Imaging Studies (OASIS): cross-sectional MRI data in young, middle aged, nondemented, and demented older adults. *J Cogn Neurosci.* 2007;19:1498-507.
- [56] Koenig LN, Day GS, Salter A, Keefe S, Marple LM, Long J, LaMontagne P, Massoumzadeh P, Snider BJ, Kanthamneni M, Raji CA, Ghoshal N, Gordon BA, Miller-Thomas M, Morris JC, Shimony JS, Benzinger TLS, Alzheimer's Disease Neuroimaging I, the Dominantly Inherited Alzheimer N. Select Atrophied Regions in Alzheimer disease (SARA): An improved volumetric model for identifying Alzheimer disease dementia. *Neuroimage Clin.* 2020;26:102248.

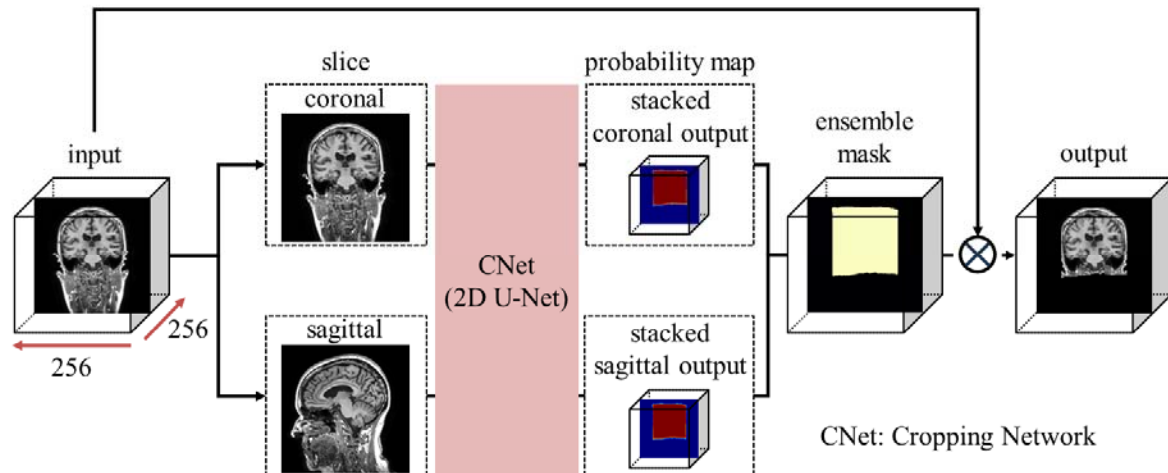
- [57] Mori S, Onda K, Fujita S, Suzuki T, Ikeda M, Zay Yar Myint K, Hikage J, Abe O, Tomimoto H, Oishi K, Taguchi J. Brain atrophy in middle age using magnetic resonance imaging scans from Japan's health screening programme. *Brain Commun.* 2022;4:fcac211.
- [58] Fujita S, Mori S, Onda K, Hanaoka S, Nomura Y, Nakao T, Yoshikawa T, Takao H, Hayashi N, Abe O. Characterization of Brain Volume Changes in Aging Individuals With Normal Cognition Using Serial Magnetic Resonance Imaging. *JAMA Netw Open.* 2023;6:e2318153.
- [59] Ronneberger O, Fischer P, Brox T. U-Net: Convolutional Networks for Biomedical Image Segmentation. *Medical Image Computing and Computer-Assisted Intervention--MICCAI 2015: 18th International Conference.* Munich, Germany: Springer; 2015:234-41.
- [60] Avesta A, Hossain S, Lin M, Aboian M, Krumholz HM, Aneja S. Comparing 3D, 2.5D, and 2D Approaches to Brain Image Auto-Segmentation. *Bioengineering (Basel).* 2023;10.
- [61] Tustison NJ, Avants BB, Cook PA, Zheng Y, Egan A, Yushkevich PA, Gee JC. N4ITK: improved N3 bias correction. *IEEE transactions on medical imaging.* 2010;29:1310-20.
- [62] Sudre CH, Cardoso MJ, Ourselin S, Alzheimer's Disease Neuroimaging I. Longitudinal segmentation of age-related white matter hyperintensities. *Med Image Anal.* 2017;38:50-64.
- [63] Altman DG, Bland JM. Measurement in Medicine: The Analysis of Method Comparison Studies. *Journal of the Royal Statistical Society Series D: The Statistician.* 2018;32:307-17.
- [64] Sun X, Xu W. Fast Implementation of DeLong's Algorithm for Comparing the Areas Under Correlated Receiver Operating Characteristic Curves. *IEEE Signal Processing Letters.* 2014;21:1389-93.
- [65] Chupin M, Gerardin E, Cuingnet R, Boutet C, Lemieux L, Lehericy S, Benali H, Garnero L, Colliot O, Alzheimer's Disease Neuroimaging I. Fully automatic hippocampus segmentation and classification in Alzheimer's disease and mild cognitive impairment applied on data from ADNI. *Hippocampus.* 2009;19:579-87.
- [66] Uchikado H, Lin W-L, DeLucia MW, Dickson DW. Alzheimer Disease With Amygdala Lewy Bodies: A Distinct Form of  $\alpha$ -Synucleinopathy. *Journal of Neuropathology & Experimental Neurology.* 2006;65:685-97.
- [67] Thompson PM, Hayashi KM, De Zubicaray GI, Janke AL, Rose SE, Semple J, Hong MS, Herman DH, Gravano D, Dordrell DM, Toga AW. Mapping hippocampal and ventricular change in Alzheimer disease. *Neuroimage.* 2004;22:1754-66.
- [68] Thompson PM, Moussai J, Zohoori S, Goldkorn A, Khan AA, Mega MS, Small GW, Cummings JL, Toga AW. Cortical variability and asymmetry in normal aging and Alzheimer's disease. *Cerebral Cortex.* 1998;8:492-509.
- [69] Nishimaki K, Ikuta K, Fujiyama S, Oishi K, Iyatomi H. PCSS: Skull Stripping With Posture Correction From 3D Brain MRI for Diverse Imaging Environment. *IEEE Access.* 2023;11:116903-18.
- [70] Ai L, Craddock RC, Tottenham N, Dyke JP, Lim R, Colcombe S, Milham M, Franco AR. Is it time to switch your T1W sequence? Assessing the impact of prospective motion correction on the reliability and quality of structural imaging. *Neuroimage.* 2021;226:117585.
- [71] Arai H, Onga Y, Ikuta K, Chayama Y, Iyatomi H, Oishi K. Disease-Oriented Image Embedding With Pseudo-Scanner Standardization for Content-Based Image Retrieval on 3D Brain MRI. *IEEE Access.* 2021;9:165326-40.

- [72] Zuo L, Liu Y, Xue Y, Dewey BE, Remedios SW, Hays SP, Bilgel M, Mowry EM, Newsome SD, Calabresi PA, Resnick SM, Prince JL, Carass A. HACA3: A unified approach for multi-site MR image harmonization. *Comput Med Imaging Graph*. 2023;109:102285.
- [73] Schwarz CG, Kremers WK, Wiste HJ, Gunter JL, Vemuri P, Sychalla AJ, Kantarci K, Schultz AP, Sperling RA, Knopman DS, Petersen RC, Jack CR, Jr., Alzheimer's Disease Neuroimaging I. Changing the face of neuroimaging research: Comparing a new MRI de-facing technique with popular alternatives. *Neuroimage*. 2021;231:117845.
- [74] Kashihara K, Imamura T. Frequency and clinical correlates of retrocollis in Parkinson's disease. *J Neurol Sci*. 2013;324:106-8.
- [75] Muller J, Wenning GK, Wissel J, Seppi K, Poewe W. Botulinum toxin treatment in atypical parkinsonian disorders associated with disabling focal dystonia. *Journal of neurology*. 2002;249:300-4.
- [76] Weiner MW, Veitch DP, Miller MJ, Aisen PS, Albala B, Beckett LA, Green RC, Harvey D, Jack CR, Jr., Jagust W, Landau SM, Morris JC, Nosheny R, Okonkwo OC, Perrin RJ, Petersen RC, Rivera-Mindt M, Saykin AJ, Shaw LM, Toga AW, Tosun D, Trojanowski JQ, Alzheimer's Disease Neuroimaging I. Increasing participant diversity in AD research: Plans for digital screening, blood testing, and a community-engaged approach in the Alzheimer's Disease Neuroimaging Initiative 4. *Alzheimers Dement*. 2023;19:307-17.
- [77] Theyers AE, Zamyadi M, O'Reilly M, Bartha R, Symons S, MacQueen GM, Hassel S, Lerch JP, Anagnostou E, Lam RW, Frey BN, Milev R, Muller DJ, Kennedy SH, Scott CJM, Strother SC, Arnott SR. Multisite Comparison of MRI Defacing Software Across Multiple Cohorts. *Frontiers in psychiatry*. 2021;12:617997.
- [78] Rubbert C, Wolf L, Turowski B, Hedderich DM, Gaser C, Dahnke R, Caspers J, Alzheimer's Disease Neuroimaging I. Impact of defacing on automated brain atrophy estimation. *Insights Imaging*. 2022;13:54.
- [79] Jaramillo SA, Felton D, Andrews L, Desiderio L, Hallarn RK, Jackson SD, Coker LH, Robinson JG, Ockene JK, Espeland MA, Women's Health Initiative Memory Study Research G. Enrollment in a brain magnetic resonance study: results from the Women's Health Initiative Memory Study Magnetic Resonance Imaging Study (WHIMS-MRI). *Acad Radiol*. 2007;14:603-12.
- [80] LeWinn KZ, Sheridan MA, Keyes KM, Hamilton A, McLaughlin KA. Sample composition alters associations between age and brain structure. *Nature communications*. 2017;8:874.
- [81] Cavallari M, Fong TG, Touroutoglou A, Dickerson BC, Schmitt E, Trivison TG, Marcantonio ER, Ngo LH, Libermann T, Pascual-Leone A, Shafi MM, Inouye SK, Jones RN, group Ss. Assessment of potential selection bias in neuroimaging studies of postoperative delirium and cognitive decline: lessons from the SAGES study. *Brain imaging and behavior*. 2022;16:1732-40.
- [82] Arslan S, Ktena SI, Makropoulos A, Robinson EC, Rueckert D, Parisot S. Human brain mapping: A systematic comparison of parcellation methods for the human cerebral cortex. *NeuroImage*. 2018;170:5-30.
- [83] Eickhoff SB, Yeo BTT, Genon S. Imaging-based parcellations of the human brain. *Nat Rev Neurosci*. 2018;19:672-86.

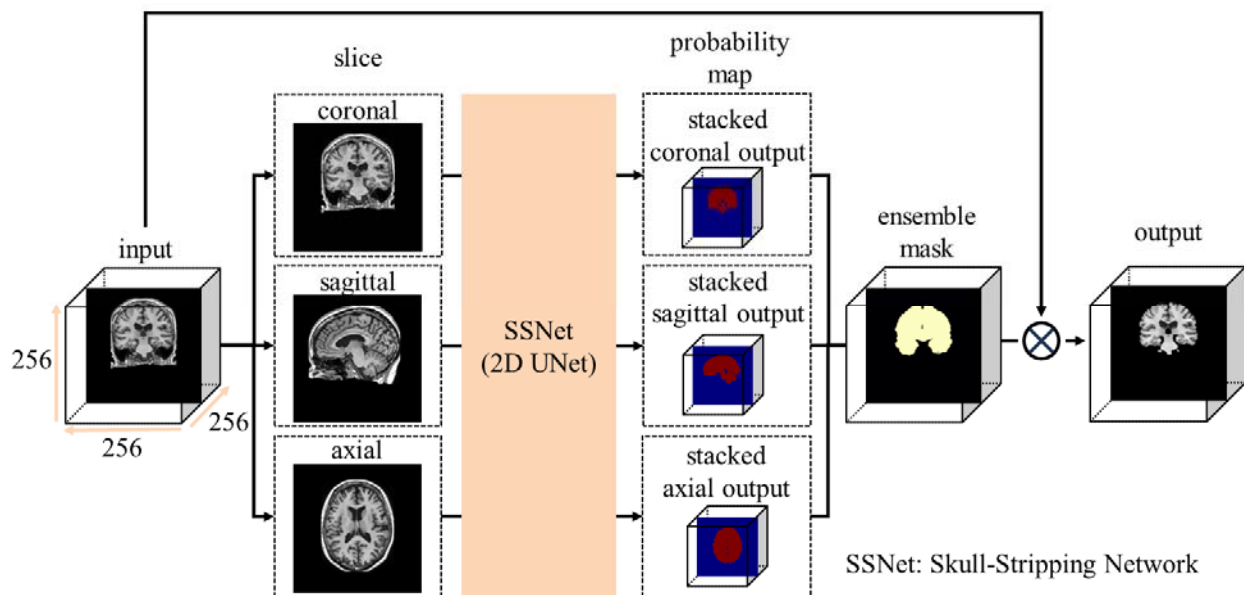
## SUPPLEMENTARY MATERIALS



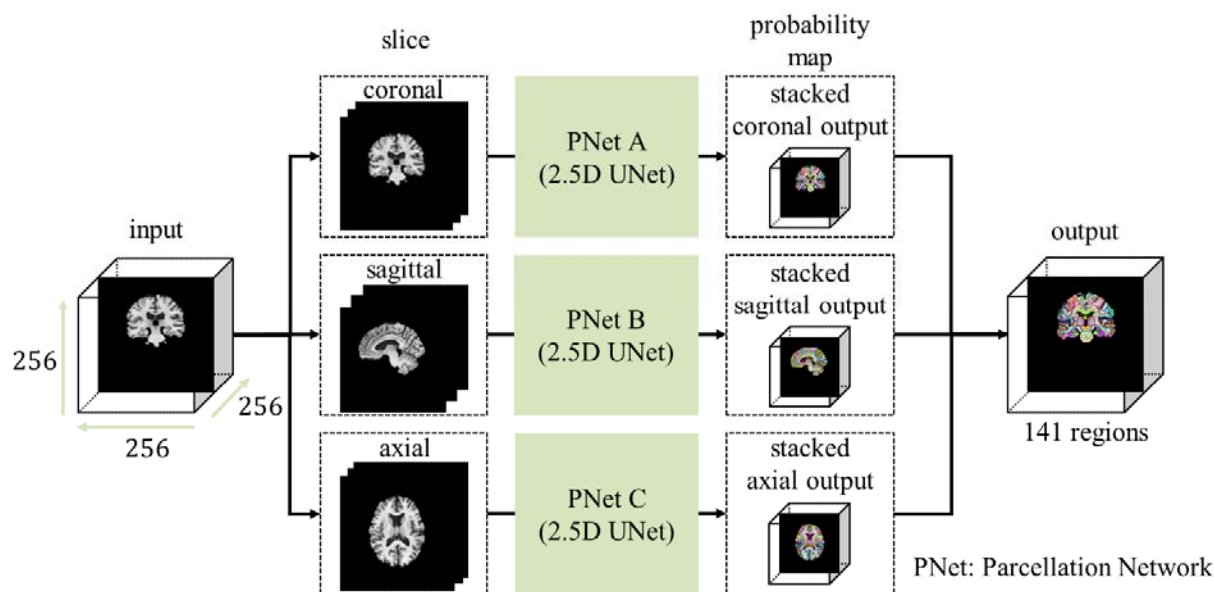
Supplementary Figure A. The procedure used to create training labels. The training labels for OpenMAP-T1 were generated by combining parcellation maps created by MALF (MRICloud).



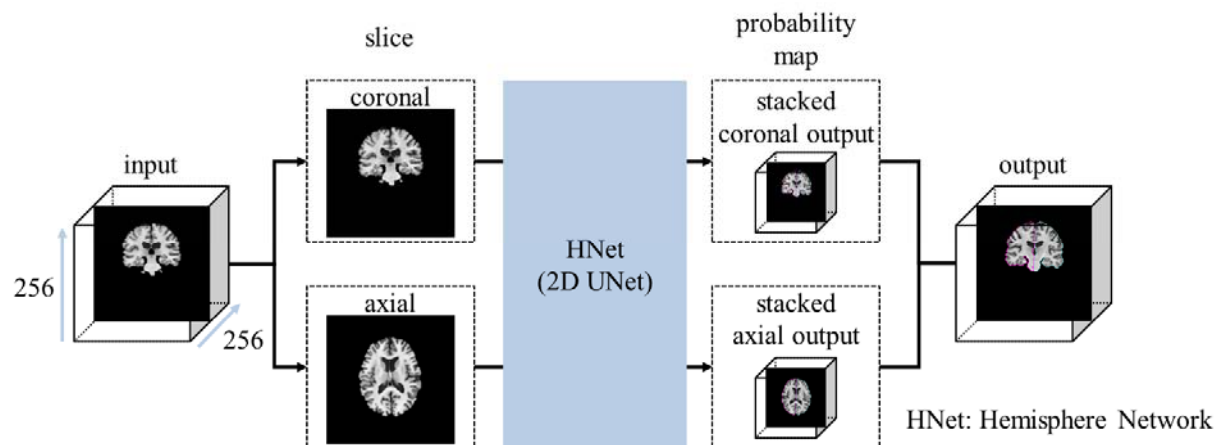
Supplementary Figure B. Overview of the cropping phase.



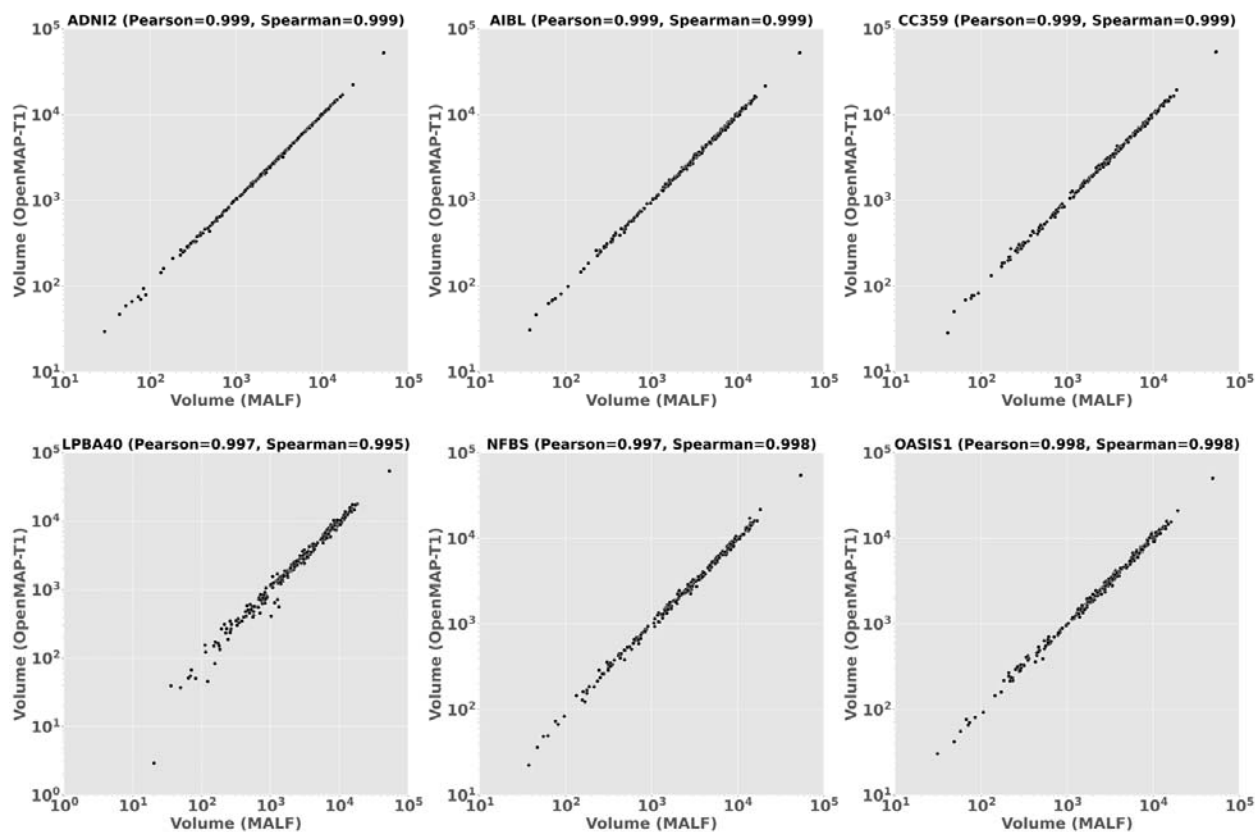
Supplementary Figure C. Overview of the skull-stripping phase.



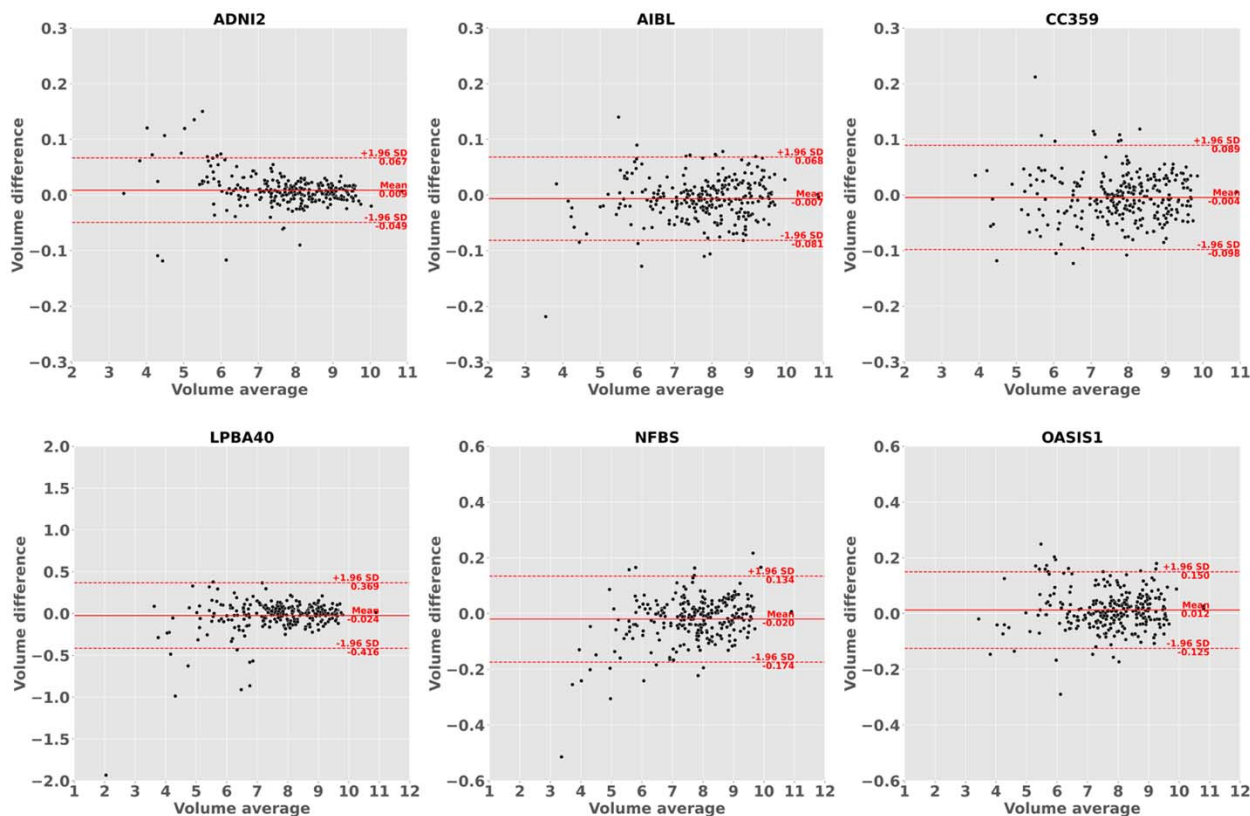
Supplementary Figure D. Overview of the parcellation phase.



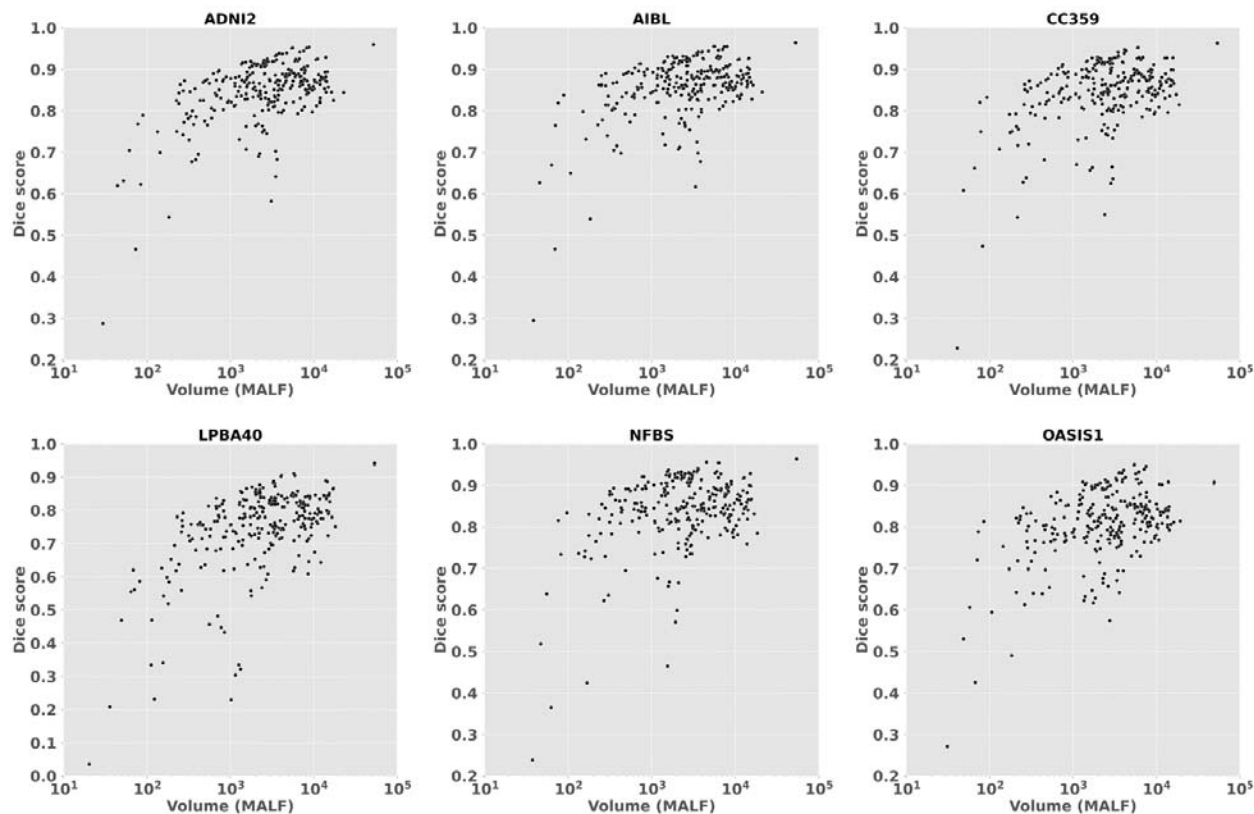
Supplementary Figure E. Overview of the hemisphere phase.



Supplementary Figure F. Correlation between the predicted volumes obtained using MALF and OpenMAP-T1 in ADNI2, AIBL, CC359, LPBA40, NFBS, and OASIS1. Note that only the LPBA40 has different scales for the x and y axes.



Supplementary Figure G. Bland-Altman plot demonstrates agreement between regional volumes predicted by MALF and OpenMAP-T1 in ADNI2, AIBL, CC359, LPBA40, NFBS, and OASIS1. The volume measurements were transformed using a base-2 logarithmic scale. Note that only the LPBA40, NFBS, and OASIS1 have different scales for the x and y axes.



Supplementary Figure H. Relationship between the predicted volumes by MALF and Dice score in ADNI2, AIBL, CC359, LPBA40, NFBS, and OASIS1. Note that only the LPBA40 has different scales for the y axes.

Table A1. Dice score and P value (ANOVA) for each effect in all datasets.

	ADNI2		ADNI3		AIBL		
	Subjects	Dice	Subjects	Dice	Subjects	Dice	
Age	<40	-	-	-	-	-	
	40s	-	-	-	-	-	
	50s	21	84.84±1.05	40	85.65±0.90	2	85.85±0.20
	60s	204	84.31±1.85	271	85.93±1.43	112	85.29±1.61
	70s	356	84.32±1.46	407	85.81±1.62	169	85.64±1.22
	80s	157	83.79±2.27	188	85.43±2.02	89	84.92±8.57
	90<	12	83.13±1.65	23	84.68±2.09	4	85.19±1.81
	p-value	p=0.001	p<0.001		p=0.797		
Sex	Female	353	84.24±1.43	486	85.81±1.25	198	85.50±1.45
	Male	397	84.18±2.04	443	85.66±2.02	178	85.21±6.12
		p-value	p=0.640	p=0.169		p=0.543	

Diagnosis	CN	259	84.11±1.92	522	85.80±1.65	268	85.63±1.24
	MCI	318	84.26±1.70	301	85.68±1.67	64	85.40±1.33
	AD	173	84.24±1.71	106	85.56±1.69	44	83.70±12.19
	p-value	p=0.553		p=0.322		p=0.023	
Field Strength	1.5T	149	83.0±1.81	-	-	102	85.10±1.48
	3.0T	601	84.50±1.64	-	-	274	85.46±4.99
	p-value	p<0.001		-		p=0.471	
Manufacturer	GE	254	83.56±1.80	211	84.98±1.96	-	-
	PHILIPS	126	84.78±1.25	142	85.91±1.67	-	-
	SIEMENS	370	84.45±1.79	576	85.97±1.45	-	-
	p-value	p<0.001		p<0.001		-	
		CC359		OASIS1		OASIS4	
		Subjects	Dice	Subjects	Dice	Subjects	Dice
Age	<40	18	83.86±1.65	2	65.53±7.58	3	82.06±1.36
	40s	80	83.41±1.89	13	81.23±3.16	5	82.89±0.99
	50s	185	84.32±2.24	22	79.64±4.99	29	83.50±1.23
	60s	72	83.85±1.65	40	81.73±2.64	169	83.18±2.15
	70s	3	80.78±6.42	83	81.13±5.48	237	83.29±2.08
	80s	1	85.79	62	79.26±9.21	111	83.12±1.70
	90<	-	-	13	80.50±8.45	16	81.88±2.05
	p-value	p=0.002		p=0.016		p=0.153	
Sex	Female	183	84.21±1.80	156	80.75±7.09	303	83.24±1.83
	Male	176	83.73±2.39	79	79.81±5.42	267	83.12±2.17
	p-value	p=0.031		p=0.300		p=0.495	
Diagnosis	CN	-	-	135	80.32±6.95		
	MCI	-	-	-	-		
	AD	-	-	100	80.59±6.07		
	p-value	-		p=0.759			
Field Strength	1.5T	179	83.96±2.34	-	-	29	81.92±1.76
	3.0T	180	83.99±1.89	-	-	541	83.25±1.98
	p-value	p=0.878		-		p<0.001	
Manufacturer	GE	120	84.99±1.46	-	-	-	-

PHILIPS	119	83.08±1.73	-	-	-	-
SIEMENS	120	83.85±2.56	-	-	-	-
p-value		p<0.001	-	-	-	-

Table A2. Dice score and p value (ANOVA) for diagnosis in OASIS4.

		OASIS4	
		Subjects	Dice
✖1 diagnosis	AD variant	10	83.85±1.08
	AD + non neurodegenerative	8	84.40±0.89
	AD / vascular	38	82.89±2.01
	AD dementia	189	83.26±1.88
	CN	39	83.38±1.71
	Dementia with Lewy Bodies (DLB)	11	83.34±1.83
	early onset AD	23	83.23±2.35
	Frontotemporal Dementia (FTD)	15	82.27±2.53
	Mild Cognitive Impairment (MCI)	41	83.24±1.73
	mood / polypharmacy / sleep	29	83.26±1.69
	non-neurodegenerative neurologic disease	19	82.45±1.96
	other - miscellaneous	15	83.00±1.84
	other non-AD neurodegenerative disorder	7	81.17±4.08
	Primary Progressive Aphasia (PPA)	7	84.00±1.04
	uncertain - AD possible	105	83.46±2.07
vascular cognitive impairment (VCI)	14	81.36±2.47	
p-value			p=0.003

Supplementary Table B. Regions of interest defined in OMAP-T1.

No.	ROI	ROI (FULL)
0	Background	Background
1	SFG_L	Superior Frontal Gyrus (Posterior Segment) Left
2	SFG_R	Superior Frontal Gyrus (Posterior Segment) Right
3	SFG_PFC_L	Superior Frontal Gyrus (Prefrontal Cortex) Left
4	SFG_PFC_R	Superior Frontal Gyrus (Prefrontal Cortex) Right
5	SFG_pole_L	Superior Frontal Gyrus (Frontal Pole) Left
6	SFG_pole_R	Superior Frontal Gyrus (Frontal Pole) Right

7	MFG_L	Middle Frontal Gyrus (Posterior Segment) Left
8	MFG_R	Middle Frontal Gyrus (Posterior Segment) Right
9	MFG_DPFC_L	Middle Frontal Gyrus (Dorsal Prefrontal Cortex) Left
10	MFG_DPFC_R	Middle Frontal Gyrus (Dorsal Prefrontal Cortex) Right
11	IFG_opercularis_L	Inferior Frontal Gyrus Pars Opercularis Left
12	IFG_opercularis_R	Inferior Frontal Gyrus Pars Opercularis Right
13	IFG_orbitalis_L	Inferior Frontal Gyrus Pars Orbitalis Left
14	IFG_orbitalis_R	Inferior Frontal Gyrus Pars Orbitalis Right
15	IFG_triangularis_L	Inferior Frontal Gyrus Pars Triangularis Left
16	IFG_triangularis_R	Inferior Frontal Gyrus Pars Triangularis Right
17	LFOG_L	Lateral Fronto Orbital Gyrus Left
18	LFOG_R	Lateral Fronto Orbital Gyrus Right
19	MFOG_L	Middle Fronto Orbital Gyrus Left
20	MFOG_R	Middle Fronto Orbital Gyrus Right
21	RG_L	Gyrus Rectus Left
22	RG_R	Gyrus Rectus Right
23	PoCG_L	Postcentral Gyrus Left
24	PoCG_R	Postcentral Gyrus Right
25	PrCG_L	Precentral Gyrus Left
26	PrCG_R	Precentral Gyrus Right
27	SPG_L	Superior Parietal Gyrus Left
28	SPG_R	Superior Parietal Gyrus Right
29	SMG_L	Supramarginal Gyrus Left
30	SMG_R	Supramarginal Gyrus Right
31	AG_L	Angular Gyrus Left
32	AG_R	Angular Gyrus Right
33	PrCu_L	Pre Cuneus Left
34	PrCu_R	Pre Cuneus Right
35	STG_L	Superior Temporal Gyrus Left
36	STG_R	Superior Temporal Gyrus Right
37	STG_pole_L	Pole of Superior Temporal Gyrus Left
38	STG_pole_R	Pole of Superior Temporal Gyrus Right
39	MTG_L	Middle Temporal Gyrus Left
40	MTG_R	Middle Temporal Gyrus Right

41	MTG_pole_L	Pole of Middle Temporal Gyrus Left
42	MTG_pole_R	Pole of Middle Temporal Gyrus Right
43	ITG_L	Inferior Temporal Gyrus Left
44	ITG_R	Inferior Temporal Gyrus Right
45	PHG_L	Parahippocampal Gyrus Left
46	PHG_R	Parahippocampal Gyrus Right
47	ENT_L	Entorhinal Area Left
48	ENT_R	Entorhinal Area Right
49	FuG_L	Fusiform Gyrus Left
50	FuG_R	Fusiform Gyrus Right
51	SOG_L	Superior Occipital Gyrus Left
52	SOG_R	Superior Occipital Gyrus Right
53	MOG_L	Middle Occipital Gyrus Left
54	MOG_R	Middle Occipital Gyrus Right
55	IOG_L	Inferior Occipital Gyrus Left
56	IOG_R	Inferior Occipital Gyrus Right
57	Cu_L	Cuneus Left
58	Cu_R	Cuneus Right
59	LG_L	Lingual Gyrus Left
60	LG_R	Lingual Gyrus Right
61	rostral_ACC_L	Rostral Anterior Cingulate Gyrus Left
62	rostral_ACC_R	Rostral Anterior Cingulate Gyrus Right
63	subcallosal_ACC_L	Subcallosal Anterior Cingulate Gyrus Left
64	subcallosal_ACC_R	Subcallosal Anterior Cingulate Gyrus Right
65	subgenual_ACC_L	Subgenual Anterior Cingulate Gyrus Left
66	subgenual_ACC_R	Subgenual Anterior Cingulate Gyrus Right
67	dorsal_ACC_L	Dorsal Anterior Cingulate Gyrus Left
68	dorsal_ACC_R	Dorsal Anterior Cingulate Gyrus Right
69	PCC_L	Posterior Cingulate Gyrus Left
70	PCC_R	Posterior Cingulate Gyrus Right
71	Insula_L	Insula Left
72	Insula_R	Insula Right
73	Amyg_L	Amygdala Left
74	Amyg_R	Amygdala Right

75	Hippo_L	Hippocampus Left
76	Hippo_R	Hippocampus Right
77	Caud_L	Caudate Nucleus Left
78	Caud_R	Caudate Nucleus Right
79	Put_L	Putamen Left
80	Put_R	Putamen Right
81	GP_L	Globus Pallidus Left
82	GP_R	Globus Pallidus Right
83	Thalamus_L	Thalamus Left
84	Thalamus_R	Thalamus Right
85	HypoThalamus_L	Hypothalamus Left
86	HypoThalamus_R	Hypothalamus Right
87	AnteriorBasalForebrain_L	Anterior Basal Forebrain Left
88	AnteriorBasalForebrain_R	Anterior Basal Forebrain Right
89	NucAccumbens_L	Nucleus Accumbens Left
90	NucAccumbens_R	Nucleus Accumbens Right
91	RedNc_L	Red Nucleus Left
92	RedNc_R	Red Nucleus Right
93	Snigra_L	Substantia Nigra Left
94	Snigra_R	Substantia Nigra Right
95	CerebellumGM_R	Cerebellum Right
96	CerebellumGM_L	Cerebellum Left
97	CP_L	Cerebral Peduncle Left
98	CP_R	Cerebral Peduncle Right
99	Midbrain_L	Midbrain Left
100	Midbrain_R	Midbrain Right
101	CST_L	Corticospinal Tract Left
102	CST_R	Corticospinal Tract Right
103	SCP_L	Superior Cerebellar Peduncle Left
104	SCP_R	Superior Cerebellar Peduncle Right
105	MCP_L	Middle Cerebellar Peduncle Left
106	MCP_R	Middle Cerebellar Peduncle Right
107	PCT_L	Pontine Crossing Tract (A Part Of MCP) Left
108	PCT_R	Pontine Crossing Tract (A Part Of MCP) Right

109	ICP_L	Inferior Cerebellar Peduncle Left
110	ICP_R	Inferior Cerebellar Peduncle Right
111	ML_L	Medial Lemniscus Left
112	ML_R	Medial Lemniscus Right
113	Pons_L	Pons Left
114	Pons_R	Pons Right
115	Medulla_L	Medulla Left
116	Medulla_R	Medulla Right
117	ACR_L	Anterior Corona Radiata Left
118	ACR_R	Anterior Corona Radiata Right
119	SCR_L	Superior Corona Radiata Left
120	SCR_R	Superior Corona Radiata Right
121	PCR_L	Posterior Corona Radiata Left
122	PCR_R	Posterior Corona Radiata Right
123	GCC_L	Genu of Corpus Callosum Left
124	GCC_R	Genu of Corpus Callosum Right
125	BCC_L	Body of Corpus Callosum Left
126	BCC_R	Body of Corpus Callosum Right
127	SCC_L	Splenium of Corpus Callosum Left
128	SCC_R	Splenium of Corpus Callosum Right
129	PVWL_L	Periventricular White Matter Posterior Lateral Left
130	PVWL_R	Periventricular White Matter Posterior Lateral Right
131	ALIC_L	Anterior Limb of Internal Capsule Left
132	ALIC_R	Anterior Limb of Internal Capsule Right
133	PLIC_L	Posterior Limb of Internal Capsule Left
134	PLIC_R	Posterior Limb of Internal Capsule Right
135	RLIC_L	Retrolenticular Part of Internal Capsule Left
136	RLIC_R	Retrolenticular Part of Internal Capsule Right
137	EC_L	External Capsule Left
138	EC_R	External Capsule Right
139	CGC_L	Cingulum (Cingulate Gyrus) Left
140	CGC_R	Cingulum (Cingulate Gyrus) Right
141	CGH_L	Cingulum (Hippocampus) Left
142	CGH_R	Cingulum (Hippocampus) Right

143	Fx/ST_L	Fornix Cres (Cres) / Stria Terminalis (cannot be resolved with current resolution) Left
144	Fx/ST_R	Fornix Cres (Cres) / Stria Terminalis (cannot be resolved with current resolution) Right
145	Fx_L	Fornix (Column and Body of Formix) Left
146	Fx_R	Fornix (Column and Body of Formix) Right
147	IFO_L	Inferior Fronto-Occipital Fasciculus Left
148	IFO_R	Inferior Fronto-Occipital Fasciculus Right
149	PTR_L	Posterior Thalamic Radiation (Include Optic Radiation) Left
150	PTR_R	Posterior Thalamic Radiation (Include Optic Radiation) Right
151	SS_L	Sagittal Stratum (Include Inferior Longitudinal Fasciculus and Inferior Fronto Occipital Fasciculus) Left
152	SS_R	Sagittal Stratum (including Inferior Longitudinal Fasciculus and Inferior Fronto Occipital Fasciculus) Right
153	SFO_L	Superior Fronto-Occipital Fasciculus (could be a part of anterior internal capsule) Left
154	SFO_R	Superior Fronto-Occipital Fasciculus (could be a part of anterior internal capsule) Right
155	SLF_L	Superior Longitudinal Fasciculus Left
156	SLF_R	Superior Longitudinal Fasciculus Right
157	CI_L	Clastrum Complex Left
158	CI_R	Clastrum Complex Right
159	PosteriorBasalForebrain_L	Posterior Basal Forebrain Left
160	PosteriorBasalForebrain_R	Posterior Basal Forebrain Right
161	Mammillary_R	Mammillary Body Right
162	Mammillary_L	Mammillary Body Left
163	LV_Frontal_L	Lateral Ventricle_Frontal Left
164	LV_body_L	Lateral Ventricle_Body Left
165	LV_atrium_L	Lateral Ventricle_Atrium Left
166	LV_Occipital_L	Lateral Ventricle_Occipital Left
167	LV_Inferior_L	Lateral Ventricle_Inferior Left
168	LV_Frontal_R	Lateral Ventricle_Frontal Right
169	LV_body_R	Lateral Ventricle_Body Right

170	LV_atrium_R	Lateral Ventricle_Atrium Right
171	LV_Occipital_R	Lateral Ventricle_Occipital Right
172	LV_Inferior_R	Lateral Ventricle_Inferior Right
173	III_ventricle	Third Ventricle
174	PVWa_L	Periventricular White Matter Frontal Left
175	PVWa_R	Periventricular White Matter Frontal Right
176	PVWp_L	Periventricular White Matter Posterior Left
177	PVWp_R	Periventricular White Matter Posterior Right
178	SFWM_L	Superior Frontal WM (Posterior Segment) Left
179	SFWM_R	Superior Frontal WM (Posterior Segment) Right
180	SFWM_PFC_L	Superior Frontal WM (Prefrontal Cortex) Left
181	SFWM_PFC_R	Superior Frontal WM (Prefrontal Cortex) Right
182	SFWM_pole_L	Superior Frontal WM (Frontal Pole) Left
183	SFWM_pole_R	Superior Frontal WM (Frontal Pole) Right
184	MFWM_L	Middle Frontal WM (Posterior Segment Left
185	MFWM_R	Middle Frontal WM (Posterior Segment Right
186	MFWM_DPFC_L	Middle Frontal WM (Dorsal Prefrontal Cortex) Left
187	MFWM_DPFC_R	Middle Frontal WM (Dorsal Prefrontal Cortex) Right
188	IFWM_opercularis_L	Inferior Frontal WM Pars Opercularis Left
189	IFWM_opercularis_R	Inferior Frontal WM Pars Opercularis Right
190	IFWM_orbitalis_L	Inferior Frontal WM Pars Orbitalis Left
191	IFWM_orbitalis_R	Inferior Frontal WM Pars Orbitalis Right
192	IFWM_triangularis_L	Inferior Frontal WM Pars Triangularis Left
193	IFWM_triangularis_R	Inferior Frontal WM Pars Triangularis Right
194	LFOWM_L	Lateral Fronto Orbital WM Left
195	LFOWM_R	Lateral Fronto Orbital WM Right
196	MFOWM_L	Middle Fronto Orbital WM Left
197	MFOWM_R	Middle Fronto Orbital WM Right
198	RGWM_L	Gyrus Rectus Left
199	RGWM_R	Gyrus Rectus Right
200	PoCWM_L	Postcentral WM Left
201	PoCWM_R	Postcentral WM Right
202	PrCWM_L	Precentral WM Left
203	PrCWM_R	Precentral WM Right

204	SPWM_L	Superior Parietal WM Left
205	SPWM_R	Superior Parietal WM Right
206	SMWM_L	Supramarginal WM Left
207	SMWM_R	Supramarginal WM Right
208	AGWM_L	Angular Gyrus WM Left
209	AGWM_R	Angular Gyrus WM Right
210	PrCuWM_L	Pre-Cuneus WM Left
211	PrCuWM_R	Pre-Cuneus WM Right
212	STWM_L	Superior Temporal WM Left
213	STWM_R	Superior Temporal WM Right
214	STWM_pole_L	Pole of Superior Temporal WM Left
215	STWM_pole_R	Pole of Superior Temporal WM Right
216	MTWM_L	Middle Temporal WM Left
217	MTWM_R	Middle Temporal WM Right
218	MTWM_pole_L	Pole of Middle Temporal WM Left
219	MTWM_pole_R	Pole of Middle Temporal WM Right
220	ITWM_L	Inferior Temporal WM Left
221	ITWM_R	Inferior Temporal WM Right
222	FuWM_L	Fusiform WM Left
223	FuWM_R	Fusiform WM Right
224	SOWM_L	Superior Occipital WM Left
225	SOWM_R	Superior Occipital WM Right
226	MOWM_L	Middle Occipital WM Left
227	MOWM_R	Middle Occipital WM Right
228	IOWM_L	Inferior Occipital WM Left
229	IOWM_R	Inferior Occipital WM Right
230	CuWM_L	Cuneus WM Left
231	CuWM_R	Cuneus WM Right
232	LGWM_L	Lingual WM Left
233	LGWM_R	Lingual WM Right
234	rostralWM_ACC_L	Rostral Anterior Cingulate WM Left
235	rostralWM_ACC_R	Rostral Anterior Cingulate WM Right
236	subcallosalWM_ACC_L	Subcallosal Anterior Cingulate WM Left
237	subcallosalWM_ACC_R	Subcallosal Anterior Cingulate WM Right

238	subgenualWM_ACC_L	Subgenual Anterior Cingulate WM Left
239	subgenualWM_ACC_R	Subgenual Anterior Cingulate WM Right
240	dorsalWM_ACC_L	Dorsal Anterior Cingulate WM Left
241	dorsalWM_ACC_R	Dorsal Anterior Cingulate WM Right
242	PCCWM_L	Pccwm Posterior Cingulate WM Left
243	PCCWM_R	Pccwm Posterior Cingulate WM Right
244	CerebellumWM_R	Cerebellum WM Right
245	CerebellumWM_L	Cerebellum WM Left
246	MCP_cb_L	Middle Cerebellar Peduncle Cerebellar Part Left
247	MCP_cb_R	Middle Cerebellar Peduncle Cerebellar Part Right
248	ICP_cb_L	Inferior Cerebellar Peduncle Cerebellar Part Left
249	ICP_cb_R	Inferior Cerebellar Peduncle Cerebellar Part Right
250	FrontSul_L	Frontal Lobe Sulcus Left
251	FrontSul_R	Frontal Lobe Sulcus Right
252	CentralSul_L	Central Sulcus Left
253	CentralSul_R	Central Sulcus Right
254	SylFrontSul_L	Sylvian Fissure Frontal Lobe Part Left
255	SylFrontSul_R	Sylvian Fissure Frontal Lobe Part Right
256	SylTempSul_L	Sylvian Fissure Temporal Lobe Part Left
257	SylTempSul_R	Sylvian Fissure Temporal Lobe Part Right
258	SylParieSul_L	Sylvian Fissure Parietal Lobe Part Left
259	SylParieSul_R	Sylvian Fissure Parietal Lobe Part Right
260	ParietSul_L	Parietal Lobe Sulcus Left
261	ParietSul_R	Parietal Lobe Sulcus Right
262	CinguSul_L	Cingular Cortex Sulcus Left
263	CinguSul_R	Cingular Cortex Sulcus Right
264	OcciptSul_L	Occipital Lobe Sulcus Left
265	OcciptSul_R	Occipital Lobe Sulcus Right
266	TempSul_L	Temporal Lobe Sulcus Left
267	TempSul_R	Temporal Lobe Sulcus Right
268	Caudate_tail_L	Caudate Tail Left
269	Fimbria_L	Fimbria Left
270	Caudate_tail_R	Caudate Tail Right
271	Fimbria_R	Fimbria Right

272	Chroid_LVetc_L	Choroid Plexus within the Lateral Ventricle Left
273	Chroid_LVetc_R	Choroid Plexus within the Lateral Ventricle Right
274	IV_ventricle	Fourth_Ventricle
275	ECCL_L	External Capsule / Claustrum Left
276	ECCL_R	External Capsule / Claustrum Right
277	ECSAnterior_L	Extracranial Space Anterior Left
278	ECSAnterior_R	Extracranial Space Anterior Right
279	ECSPosterior_L	Extracranial Space Posterior Left
280	ECSPosterior_R	Extracranial Space Posterior Right

---